An unconstrained DFT approach to microphase formation and application to binary Gaussian mixtures

Davide Pini, Alberto Parola, and Luciano Reatto

Articles you may be interested in

Mixtures of ions and amphiphilic molecules in slit-like pores: A density functional approach
J. Chem. Phys. **142**, 164703 (2015); 10.1063/1.4918640

Decay of correlation functions in hard-sphere mixtures: Structural crossover
J. Chem. Phys. **121**, 7869 (2004); 10.1063/1.1798057

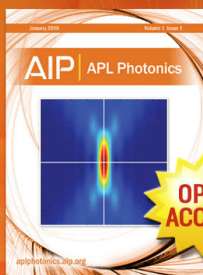Structure of nonuniform fluid mixtures: A self-consistent density-functional approach
J. Chem. Phys. **117**, 8933 (2002); 10.1063/1.1514650

Phase behavior and structure of star-polymer–colloid mixtures
J. Chem. Phys. **116**, 9518 (2002); 10.1063/1.1474578

Density-functional studies of amphiphilic binary mixtures. I. Phase behavior
J. Chem. Phys. **113**, 4476 (2000); 10.1063/1.1288269

An unconstrained DFT approach to microphase formation and application to binary Gaussian mixtures

Davide Pini,[1,a)] Alberto Parola,[2] and Luciano Reatto[3]
[1]*Dipartimento di Fisica, Università degli Studi di Milano, Via Celoria 16, 20133 Milano, Italy*
[2]*Dipartimento di Scienza ed Alta Tecnologia, Università dell'Insubria, Via Valleggio 11, 22100 Como, Italy*
[3]*Via Bazzini 20, 20133 Milano, Italy*

The formation of microphases in systems of particles interacting by repulsive, bounded potentials is studied by means of density-functional theory (DFT) using a simple, mean-field-like form for the free energy which has already been proven accurate for this class of soft interactions. In an effort not to constrain the configurations available to the system, we do not make any assumption on the functional form of the density profile $\rho(\mathbf{r})$, save for its being periodic. We sample $\rho(\mathbf{r})$ at a large number of points in the unit cell and minimize the free energy with respect to both the values assumed by $\rho(\mathbf{r})$ at these points *and* the lattice vectors which identify the Bravais lattice. After checking the accuracy of the method by applying it to a one-component generalized exponential model (GEM) fluid with pair potential $\epsilon \exp[-(r/R)^4]$, for which extensive DFT and simulation results are already available, we turn to a binary mixture of Gaussian particles which some time ago was shown to support microphase formation [A. J. Archer, C. N. Likos, and R. Evans, J. Phys.: Condens. Matter **16**, L297 (2004)], but has not yet been investigated in detail. The phase diagram which we obtain, that supersedes the tentative one proposed by us in a former study [M. Carta, D. Pini, A. Parola, and L. Reatto, J. Phys.: Condens. Matter **24**, 284106 (2012)], displays cluster, tubular, and bicontinuous phases similar to those observed in block copolymers or oil/water/surfactant mixtures. Remarkably, bicontinuous phases occupy a rather large portion of the phase diagram. We also find two non-cubic phases, in both of which one species is preferentially located inside the channels left available by the other, forming helices of alternating chirality. The features of cluster formation in this mixture and in GEM potentials are also compared. © 2015 AIP Publishing LLC. [http://dx.doi.org/10.1063/1.4926469]

I. INTRODUCTION

One of the main reasons for the current interest in soft matter is its ability to self-assemble into complex states and the possibility to steer this process towards the formation of a chosen structure by acting on the parameters which control the effective interactions between its building blocks. A remarkable and widely acknowledged instance of this ability is the occurrence of microphases, i.e., inhomogeneous phases displaying periodic density modulations whose characteristic length, although being larger than the size of the particles, cannot nevertheless be considered macroscopic.[1] For example, microphases are formed in block copolymer melts[2] and in solutions of amphiphilic molecules in a solvent consisting of two immiscible species, one of which is polar and the other one apolar.[3] In these systems, the monomers of different species, or the hydrophilic and hydrophobic parts of the molecules, have a tendency to segregate in two separate macroscopic regions, but the intramolecular bonds prevent macroscopic phase separation from taking place. The ensuing competition leads to a host of different particle arrangements, in which density modulations may take place along one, two, or three spatial directions, such as lamellar, tubular, and cluster phases, respectively. For

triply periodic structures, more exotic configurations are also possible, including bicontinuous phases.[4]

A similar mechanism is at play also in fluids consisting of hard-core spherical particles with short-range attractive and longer-ranged repulsive interactions. Here, the attractive part of the potential favors particle aggregation, whereas the repulsive part imposes an energy penalty on the growth of a macroscopic dense phase. When the competition between attraction and repulsion is strong enough, the gas-liquid phase transition is suppressed, and the phase diagram of the fluid has been shown to present microphases in both two[5–7] and three dimensions.[8–10]

Irrespective of its specific nature, the attitude of a one-component system to form microphases ultimately rests upon a property of the effective interaction between its constituents: if the Fourier transform of the interaction has a negative minimum at some non-vanishing wave vector k, then density modulations with characteristic length $d \sim 2\pi/k$ will be strongly favored over the other Fourier components of the density profile and can lead to inhomogeneous phases under suitable thermodynamic conditions.[1] Another instance of this rather general scenario which has gained considerable attention in recent times is cluster formation in particles interacting via isotropic, bounded repulsive potentials of ultrasoft type such that not only are the overlaps between particles allowed but also the resulting energy

a)Electronic address: davide.pini@fisica.unimi.it

penalty is very low.[11–13] At high enough density, these systems form crystal phases, whose lattice sites are occupied by clusters of many particles, at variance with the single-particle occupancy of atomic crystals. The theoretical investigation of these phases has brought forth many remarkable properties, the most prominent of which is that a change in the density of the crystal is achieved by changing the average number of particles in a cluster, while leaving the lattice constant almost unchanged.[11,12] The reason of the existence of such an intrinsic characteristic length may not be obvious by looking at the potential in real space, but is again revealed by the negative minimum of its Fourier transform at $k \neq 0$. The link between the occurrence of this minimum and the formation of cluster phases in fluids of soft, repulsive particles has been shown explicitly, and potentials of this kind have been labeled as belonging to the class of $Q^{\pm}$ interactions.[14] They come along, for instance, in the modelization of the effective interactions between amphiphilic dendrimers.[15,16]

The $Q^{\pm}$ class does not include the prototypical repulsive soft-core interaction, namely, the Gaussian potential, which has been adopted to represent the effective pair interactions between linear polymers[17,18] and non-amphiphilic dendrimers.[19] For the interaction strengths relevant to these systems, its phase diagram does not exhibit ordered states. However, it was pointed out that ordered cluster phases in Gaussian potentials can still occur if one turns to *mixtures* of Gaussian particles with suitably chosen interaction parameters. Two such cases were considered in Refs. 20 and 24. In Ref. 20, a binary mixture with interaction strengths and ranges appropriate to model linear polymers[21–23] was modified by decreasing the range of the interaction between different species. In Ref. 24, the interaction parameters were chosen so as to model a binary mixture of dendrimers, with one species being much more compact than the other. In general, cluster formation is favored by negative non-additivity of the interaction ranges.

The purpose of those studies was not so much to undertake a detailed description of the phase diagram but to show that microphases are possible. As an example of the phases which may occur, in Ref. 20, a cluster crystal with the CsCl structure was considered, and by employing density-functional theory (DFT), it was shown that this structure has indeed a lower free energy than that of the homogeneous fluid in a certain region of the density-concentration plane. At the same time, it was clearly stated that such a configuration was not meant to exhaust all the phases presented by the mixture in the inhomogeneous region and that "a rich variety of one-, two-, or three-dimensionally modulated structures (cylinders, lamellae, and crystals), similar to that encountered in block copolymer blends or in ternary oil/water/surfactant mixtures could be expected."[24]

This possibility deserves to be ascertained, and in the present paper, we do so by studying in detail via DFT the phase diagram of the same model Gaussian mixture considered in Ref. 20. To this purpose, we have used the same free-energy functional adopted in that study, but in such a way as to allow the system the freedom to arrange into phases different from the aforementioned CsCl crystal. There are two possible strategies to accomplish this program: one consists in selecting a suitably large pool of crystal structures and

parameterizing their density profile by a given functional form depending on a small number of free parameters. A widely adopted choice, suitable for localized crystal phases such as those formed by the aforementioned $Q^{\pm}$ interactions, consists in a sum of Gaussians centered at the sites of a specified lattice. At a given thermodynamic state, the free-energy functional is minimized with respect to these parameters for each of the candidate structures and the one which gives the lowest free energy is selected.

We deemed the above approach unsuitable to the system in hand for a number of reasons. First, our insight into its behavior was admittedly too poor, to enable us to make a reasonable guess as to which structures should be allowed into the contest and which ones should instead be discarded *a priori*. Moreover, even assuming that one uses as a guide the suggestion of Ref. 24 concerning the structures found in block copolymers or in oil/water/surfactant mixtures, a new difficulty has to be faced, stemming from the fact that several of those structures display bicontinuous phases, which do not lend themselves to being represented as a superposition of functions centered at the sites of a simple Bravais lattice. In this case, it is more useful to resort to an expansion on a set of basis functions, which have the symmetries of the phase being investigated.[25,26] For instance, they may consist of a superposition of plane waves with wave vectors in a given subset of the reciprocal lattice. However, this still requires these symmetries to be specified in advance. In addition, in the study of microphases, it often occurs that phases which have different symmetries and cannot be mistaken for one another have nevertheless very similar free energies. In such a situation, one cannot rule out the possibility that imposing a given functional form to the density profile might alter the close contest between the various structures and artificially enhance the stability of some of them at the expense of the truly stable one.

These reasons lead us to the other approach to the minimization of the free-energy functional, namely, not to make any *ansatz* as to the functional form of the density profile or the kind of lattice and perform instead an unconstrained minimization, whereby the density profile is discretized by considering its values on a suitably large number of points inside a certain domain, and the free-energy functional is minimized with respect to these values. This is of course quite an obvious idea, so one might wonder why it is not always adopted. The equally obvious answer is that while this program has been successfully accomplished in the study of microphase formation in two-dimensional fluids,[7] it still remains rather problematic when it comes to three-dimensional fluids with triply periodic density modulations. One difficulty is due to the fact that in three dimensions, a discretization with the basic requirement that a region with the characteristic size of a particle should contain several grid points along each axis results in a very large total number of points, typically $\sim 10^6$. With such a large number of independent variables, convergence to a minimum of the free-energy functional can be disappointingly slow. The other main hindrance related to handling a large number of variables is that in a situation such as the occurrence of microphases, in which the free-energy functional is not globally convex, the number of local minima is expected to grow enormously.[27] As a consequence, the minimization stands very

high chances of getting stuck in some state with defects, especially if the size of the domain, where the density profile is sampled, does not match the period of the structures which the system would form spontaneously. The above difficulties resemble those which have to be faced in numerical simulations, to the point that it could even be questioned whether such a method would offer any real advantage with respect to simulation.

As far as the former problem is concerned, in a preliminary investigation of the same mixture studied here which we made few years ago,[28] we found that the speed of convergence of the algorithm could be increased enough to make it of practical use by adopting well-established techniques for the minimization of functions of many variables,[29] notably a careful choice of the direction and size of each minimization step. Nevertheless, the latter problem was still there: while one- and two-dimensional periodic microphases were easily obtained, the tendency of the system to form defective structures made the search of triply periodic microphases very inefficient. The feasibility of a purely numerical minimization in three dimensions was in fact already shown in the application of the self-consistent field theory (SCFT) originally developed for block copolymers[2,25] to amphiphilic molecules[30] and particles with competing attractive and repulsive interactions.[10] In those studies, the frequent occurrence of defective structures was also remarked.

In order to cope with this issue, in the present paper, we have adopted an idea borrowed from numerical simulation: following the method of Parrinello and Rahman,[31] we have assumed from the outset that the density profile is periodic and regarded the vectors which define the Bravais lattice as quantities to be determined by the minimization, on the same footing as the values of the density profile in the unit cell. We must observe that the use of this idea in functional minimization has been already put forth, again in the context of SCFT for block copolymers,[32,33] where its relationship with the method of Parrinello and Rahman was pointed out.[33] This procedure has been applied many times to microphase formation in block copolymers[34–36] and also in non-polymeric systems.[37] Here, we have implemented a similar method along with the spatial discretization of the density profile in three dimensions and used it to carry out DFT minimization.

The comparison with the results of our previous study[28] shows that the improvements brought by the present method are remarkable: on the one hand, defective structures are outright eliminated and on the other hand, many periodic configurations come about, which we had failed to detect before. In fact, the phase portrait which we have obtained here is quite different and much richer than that reported in our former work. As anticipated in Ref. 24, most of its phases resemble those found in block copolymers or oil/water/surfactant mixtures. Actually, except for the lamellar, one-dimensionally modulated phase that is always superseded by others, the phase diagram reported here contains all the phases commonly predicted in block copolymer melts[25,26,38] including tubular and bicontinuous structures such as the gyroid and the double diamond. In addition, we have obtained an orthorhombic phase which was found experimentally[39,40] and predicted[34] much later than the aforementioned ones, as well as a tetragonal phase which, to our knowledge, has

not been predicted theoretically before. In both of them, one species forms a rather loose lattice with wide channels and the other is preferentially located inside these channels, where it forms helices of alternating chirality.

A feature shared by all the phases which we have obtained is that the simultaneous localization of both species at the sites of a simple lattice never occurs, since one or even both species percolate through the voids left available by the other. Overall, bicontinuous phases occupy a significant part of the phase diagram. Far from being simply a test bed of our method, Gaussian mixtures appear then to be interesting in their own sake, as the presence of bicontinuous phases is of interest for a number of applications.[41]

The above results suggest that the minimization algorithm developed here may be useful in many situations in which periodic structures are formed, especially when the translational invariance is broken spontaneously and the system is allowed the freedom to choose the periodicity. Since the underlying assumption is that the density profile is periodic, this method is of course unsuited to the study of confined systems or to situations in which one is actually interested in defective configurations.

The plan of the paper is as follows: the general features of the method used to minimize the free-energy functional are described in Sec. II. Before considering the application to the Gaussian mixture, we test the accuracy of the method in Sec. III, by applying it to a one-component system whose interaction belongs to the $Q^{\pm}$ class and for which extensive DFT and simulation results are already available, namely, the generalized exponential model (GEM).[11,12] In Sec. IV, we introduce the Gaussian mixture which is the object of this study, give a sufficient condition on the interaction parameters for microphases to occur, and discuss some aspects of the correlations and effective interactions in the homogeneous region which we regard as relevant to the mechanism leading to microphases. The results obtained by applying DFT to this mixture are contained in Sec. V, where we display the phase diagram of the system and describe the qualitative features of the phases which we have found. For the phase where one of the species forms localized clusters, the density dependence of their population, mutual distance, and localization is compared with the corresponding properties of the GEM fluid. The main conclusions that we draw from this investigation, its limits, and possible directions for future work are outlined in Sec. VI. Some technical details pertaining to the minimization algorithm are described in the Appendix.

II. THEORY

A. The density functional and the λ-line

In the present paper, we will be studying a binary mixture of particles interacting by a two-body, bounded repulsive potential $w_{\alpha\gamma}(r)$, where r is the interparticle distance and $\alpha, \gamma = 1, 2$ identify the particle species. In order to deal with the inhomogeneous phases, a simple perturbative DFT in the grand canonical ensemble has been adopted throughout. The system in study is obtained by adding to an unperturbed or "reference" system, whose properties are assumed to be

known, an interaction which is regarded as a perturbation. The "excess" contribution to the free-energy functional due to the perturbation is treated in mean-field approximation, by neglecting correlations between the particles. For the soft-core systems considered here, such that the two-body potential

does not contain any singular part, it is natural to identify the perturbation with the full interaction, and the unperturbed system with a binary mixture of ideal gases, whose free-energy functional is of course known exactly. The grand potential functional $\Omega[\rho_1(\mathbf{r}), \rho_2(\mathbf{r})]$ is then

$$\beta\Omega[\rho_1(\mathbf{r}), \rho_2(\mathbf{r})] = \beta F_{id}[\rho_1(\mathbf{r}), \rho_2(\mathbf{r})] + \beta F_{ex}[\rho_1(\mathbf{r}), \rho_2(\mathbf{r})] - \sum_{\alpha=1}^{2} \beta\mu_\alpha \int d^3\mathbf{r}\, \rho_\alpha(\mathbf{r})$$

$$= \sum_{\alpha=1}^{2} \int d^3\mathbf{r}\, \rho_\alpha(\mathbf{r}) \left\{ \ln[\rho_\alpha(\mathbf{r})\Lambda_\alpha^3] - 1 - \beta\mu_\alpha \right\} + \frac{1}{2} \sum_{\alpha,\gamma=1}^{2} \int d^3\mathbf{r} \int d^3\mathbf{r}' \rho_\alpha(\mathbf{r})\rho_\gamma(\mathbf{r}')\beta w_{\alpha\gamma}(\mathbf{r}-\mathbf{r}'), \quad (1)$$

where F_{id} and F_{ex} are, respectively, the ideal and excess parts of the Helmholtz free energy, $\beta = 1/k_BT$, T being the absolute temperature and k_B the Boltzmann constant, $\rho_\alpha(\mathbf{r})$ is the density profile of species α, μ_α is the chemical potential, and $\Lambda_\alpha = h/\sqrt{2\pi m_\alpha k_B T}$ is the thermal wavelength, m_α being the mass of the particle. The use of functional (1) to describe non-uniform phases of soft-core particles has been justified in detail in Ref. 12, at least for one-component systems. A similar mean-field approach has also been employed in the study of microphase formation in a fluid of hard-core particles with competing short-range attractive and longer-range repulsive interactions;[7,42] although in the latter case, the reference part of the free energy contains also the hard-sphere contribution and therefore cannot be treated exactly.

For given chemical potentials μ_α, the equilibrium density profiles $\rho_\alpha(\mathbf{r})$ are obtained by minimizing functional (1). This requires that $\rho_\alpha(\mathbf{r})$ satisfies the Euler-Lagrange equations $\delta(\beta\Omega)/\delta\rho_\alpha(\mathbf{r}) = 0$. A homogeneous state such that $\rho_\alpha(\mathbf{r})$ is identically equal to the average number density $\bar{\rho}_\alpha$ is a trivial solution of the Euler-Lagrange equations with chemical potential

$$\beta\mu_\alpha = \ln(\bar{\rho}_\alpha \Lambda_\alpha^3) + \sum_{\gamma=1}^{2} \bar{\rho}_\gamma \int d^3\mathbf{r}\, \beta w_{\alpha\gamma}(\mathbf{r}). \quad (2)$$

However, such a stationary solution does not necessarily correspond to a minimum. For this to be the case, the additional condition of stability of $\bar{\rho}_\alpha$ with respect to small perturbations $\delta\rho_\alpha(\mathbf{r})$ has to be satisfied. This amounts to the constraint

$$\sum_{\alpha,\gamma=1}^{2} \int d^3\mathbf{r} \int d^3\mathbf{r}' c_{\alpha\gamma}(\mathbf{r},\mathbf{r}')\delta\rho_\alpha(\mathbf{r})\delta\rho_\gamma(\mathbf{r}') < 0, \quad (3)$$

where we have introduced the direct correlation function $c_{\alpha\gamma}(\mathbf{r},\mathbf{r}')$ given by

$$c_{\alpha\gamma}(\mathbf{r},\mathbf{r}') \equiv \left. \frac{\delta^2(-\beta\Omega)}{\delta\rho_\alpha(\mathbf{r})\delta\rho_\gamma(\mathbf{r}')} \right|_{\bar{\rho}_\alpha, \bar{\rho}_\gamma}. \quad (4)$$

We remark that, according to the definition above, $c_{\alpha\gamma}(\mathbf{r},\mathbf{r}')$ includes the ideal-gas contribution. For a homogeneous state, one has $c_{\alpha\gamma}(\mathbf{r},\mathbf{r}') = c_{\alpha\gamma}(\mathbf{r}-\mathbf{r}')$, and Eq. (3) is equivalent to requiring that the matrix with elements $\tilde{c}_{\alpha\gamma}(\mathbf{k})$ be negative definite for every $\mathbf{k}$, where we have used the tilde to denote

the Fourier transform with respect to $\mathbf{r}$,

$$\tilde{c}_{\alpha\gamma}(\mathbf{k}) = \int d^3\mathbf{r}\, e^{-i\mathbf{k}\cdot\mathbf{r}} c_{\alpha\gamma}(\mathbf{r}). \quad (5)$$

Equation (1) gives the direct correlation function in random-phase approximation (RPA),

$$\tilde{c}_{\alpha\gamma}(k) = -\frac{\delta_{\alpha\gamma}}{\bar{\rho}_\alpha} - \beta\tilde{w}_{\alpha\gamma}(k), \quad (6)$$

where k is the modulus of $\mathbf{k}$, and $\delta_{\alpha\gamma}$ is the Kronecker delta.

If $\tilde{c}_{\alpha\gamma}(k) < 0$ for every k, as is the case with the Gaussian potential that will be considered in Secs. IV and V, the above condition reduces to

$$\det \|\tilde{c}_{\alpha\gamma}(k)\| > 0 \qquad \text{for every } k, \quad (7)$$

where det indicates the determinant. A violation of this condition for a certain homogeneous state $\bar{\rho}_1$, $\bar{\rho}_2$, and wave vector k means that such a state is unstable with respect to density fluctuations with characteristic length $d \sim 2\pi/k$. The situation most commonly encountered has the violation of the stability condition at $k = 0$ and this corresponds to the spinodal instability, which leads to separation into two bulk phases with different densities for each of the two species. In this case, the boundary between the thermodynamic states for which condition (7) is satisfied and those for which it is violated is the spinodal line, which is given by the locus of densities $\bar{\rho}_1$ and $\bar{\rho}_2$ such that

$$\det \|\tilde{c}_{\alpha\gamma}(k = 0)\| = 0. \quad (8)$$

Here, on the other hand, we are interested in the situation in which the spinodal instability does not occur and is replaced by an instability at non-vanishing k, i.e., by density modulations whose wavelength, while being larger than the characteristic size of the particles, cannot nevertheless be considered macroscopic — the inhomogeneous phases being then referred to as microphases. The stability boundary is then identified by the so-called λ-line, which is determined by the locus,[20]

$$\det \|\tilde{c}_{\alpha\gamma}(k)\| = 0, \quad (9)$$

$$\frac{d}{dk} \det \|\tilde{c}_{\alpha\gamma}(k)\| = 0, \quad (10)$$

for some $k \neq 0$.

While inside the region of the T-$\bar\rho_1$-$\bar\rho_2$ space bounded by the λ-line the system is necessarily found in an inhomogeneous state, the line of the phase diagram which separates the homogeneous states from the inhomogeneous ones does not in general coincide with the λ-line, just as the fluid-fluid coexistence region does not in general coincide with the spinodal line. In fact, stability condition (7) guarantees that a homogeneous state is a *local* minimum of the grand potential functional Ω for μ_1 and μ_2 given by Eq. (2). This, however, does not necessarily coincide with the *global* minimum at the same μ_1 and μ_2. Even more importantly, knowing that for some states, the system displays density modulations with a certain characteristic length says almost nothing on the kind of configurations into which the particles are expected to arrange or which of them is the most stable. In order to address these issues and thus obtain the *bona fide* phase diagram of the mixture, one has to look for the non-trivial minima of functional (1). In the remainder of the section, we will describe the method that we adopted to this purpose.

B. Minimization method

Our basic *assumption* is that the density profiles $\rho_\alpha(\mathbf{r})$ are periodic functions of $\mathbf{r}$. Therefore, we have

$$\rho_\alpha(\mathbf{r} + \mathbf{a}_i) = \rho_\alpha(\mathbf{r}),\qquad(11)$$

where $\mathbf{a}_i$, $i = 1, 2, 3$, are a set of vectors defining a Bravais lattice. We indicate by $\mathbf{A}$ the matrix obtained by arranging the vectors $\mathbf{a}_i$ into columns

$$A \equiv (\mathbf{a}_1, \mathbf{a}_2, \mathbf{a}_3).\qquad(12)$$

A generic point $\mathbf{R_l}$ of the lattice is then given by $\mathbf{R_l} = \mathbf{A} \cdot \mathbf{l}$, where $\mathbf{l}$ is a vector with integer components $l_i = 0, \pm 1, \pm 2 \ldots$. Similarly, a point in the unit cell is given by $\mathbf{x} = \mathbf{A} \cdot \mathbf{s}$, where $\mathbf{s}$ is a vector with components s_i in the interval $-1/2 \le s_i < 1/2$. By suitably choosing $\mathbf{l}$ and $\mathbf{x}$, any point $\mathbf{r}$ of the continuum space can be expressed as $\mathbf{r} = \mathbf{R_l} + \mathbf{x}$.

Since $\rho_\alpha(\mathbf{r})$ is periodic, the integrand in the ideal-gas term F_{id} in Eq. (1) gives the same contribution for each cell, so that we have

$$\frac{\beta F_{\text{id}}}{V} = \frac{1}{v} \sum_{\alpha=1}^{2} \int_v d^3\mathbf{x}\, \rho_\alpha(\mathbf{x}) \left\{ \ln[\rho_\alpha(\mathbf{x})\Lambda_\alpha^3] - 1 \right\},\quad(13)$$

where V is the volume of the system, and $v = |\det \mathbf{A}|$ is the volume of the unit cell. In the following, we will use Eq. (2) to parameterize the chemical potential μ_α. We then obtain

$$\ln[\rho_\alpha(\mathbf{x})\Lambda_\alpha^3] - 1 - \beta\mu_\alpha = \ln[\rho_\alpha(\mathbf{x})/\bar\rho_\alpha] - 1 - \beta\mu_\alpha^{\text{ex}},\quad(14)$$

where $\beta\mu_\alpha^{\text{ex}} \equiv \beta\mu_\alpha - \ln(\bar\rho_\alpha\Lambda_\alpha^3)$ is given by the summation in the rhs of Eq. (2). By doing so, the thermal wavelength Λ_α does not appear anymore.

The integrand in the excess free energy F_{ex}, unlike that in F_{id}, is not periodic, because the potential $w_{\alpha\gamma}(\mathbf{r})$ is not. However, we can rewrite F_{ex} by expanding ρ_α in a Fourier series,

$$\rho_\alpha(\mathbf{x}) = \frac{1}{v} \sum_{\mathbf{m}} e^{-i\mathbf{k_m}\cdot\mathbf{x}} \check\rho_{\mathbf{m},\alpha},\qquad(15)$$

where $\mathbf{k_m}$, $m_i = 0, \pm 1, \pm 2 \ldots$ is a vector of the reciprocal lattice. The expansion coefficients $\check\rho_{\mathbf{m},\alpha}$ are given by

$$\check\rho_{\mathbf{m},\alpha} = \int_v d^3\mathbf{x}\, e^{i\mathbf{k_m}\cdot\mathbf{x}} \rho_\alpha(\mathbf{x}).\qquad(16)$$

Here, as well as in Eq. (13), the integration domain is the unit cell rather than the whole space as in Eqs. (1) and (5). By substituting Eq. (16) in the excess Helmholtz free energy F_{ex} given in Eq. (1) and taking into account that $\mathbf{R_l} \cdot \mathbf{k_m}$ is an integer multiple of 2π because of the relationship between the direct and reciprocal lattices, we obtain

$$\frac{\beta F_{\text{ex}}}{V} = \frac{1}{2v^2} \sum_{\mathbf{m},\alpha,\gamma} \check\rho_{\mathbf{m},\alpha}\, \check\rho_{-\mathbf{m},\gamma}\, \beta\tilde w_{\alpha\gamma}(\mathbf{k_m}).\qquad(17)$$

Equation (17) is the straightforward generalization to a mixture of the expression of F_{ex} obtained in Eq. (40) of Ref. 12, where the same mean-field functional adopted here was used to study cluster formation in a fluid of particles interacting by a GEM potential. However, in that investigation, $\rho(\mathbf{r})$ was represented as a superposition of Gaussians centered at the sites of a specified lattice, while in the present study, we aim at releasing this assumption.

To this end, the density profile is discretized as $\rho_{\mathbf{n},\alpha} \equiv \rho_\alpha(\mathbf{x_n})$ by sampling it at a discrete set of N^3 points of the unit cell, $\mathbf{x_n} = \mathbf{A} \cdot \mathbf{s_n}$, with $\mathbf{s_n} = \mathbf{n}/N$ and $n_i = 0, \pm 1, \pm 2 \ldots$ such that $-N/2 \le n_i < N/2$, N being an (even) integer. Because of the discretization, the ideal-gas term F_{id} in Eq. (13) and the Fourier integral in Eq. (16) are replaced by the discrete sums F_{id}^{D} and $\check\rho_{\mathbf{m},\alpha}^{\text{D}}$ given by

$$\frac{\beta F_{\text{id}}^{\text{D}}}{V} = \frac{1}{N^3} \sum_{\mathbf{n},\alpha} \rho_{\mathbf{n},\alpha} \left[\ln(\rho_{\mathbf{n},\alpha}\Lambda_\alpha^3) - 1 \right],\qquad(18)$$

$$\check\rho_{\mathbf{m},\alpha}^{\text{D}} = \frac{v}{N^3} \hat\rho_{\mathbf{m},\alpha},\qquad(19)$$

where $\hat\rho_{\mathbf{m},\alpha}$ is given by

$$\hat\rho_{\mathbf{m},\alpha} = \sum_{\mathbf{n}} e^{2\pi i \mathbf{m}\cdot\mathbf{n}/N} \rho_{\mathbf{n},\alpha}.\qquad(20)$$

Similarly, we have

$$\rho_{\mathbf{n},\alpha} = \frac{1}{N^3} \sum_{\mathbf{m}} e^{-2\pi i \mathbf{n}\cdot\mathbf{m}/N} \hat\rho_{\mathbf{m},\alpha}.\qquad(21)$$

Unlike in Eqs. (15) and (17), the sums in Eqs. (18), (20), and (21) are carried out in the finite interval $-N/2 \le m_i, n_i < N/2$. If Eq. (19) is substituted in Eq. (17) for F_{ex} and Eqs. (18) and (14) for F_{id} are used, the functional Ω is replaced by a discretized functional Ω_{D} such that the grand potential per unit volume $\omega_{\text{D}} \equiv \Omega_{\text{D}}/V$ is a function of the discretized densities $\rho_{\mathbf{n},\alpha}$,

$$\beta\omega_{\text{D}}(\rho_{\mathbf{n},\alpha}) = \frac{1}{N^3} \sum_{\mathbf{n},\alpha} \rho_{\mathbf{n},\alpha} \left[\ln(\rho_{\mathbf{n},\alpha}/\bar\rho_\alpha) - 1 - \beta\mu_\alpha^{\text{ex}} \right]$$
$$+ \frac{1}{2N^6} \sum_{\mathbf{m},\alpha,\gamma} \hat\rho_{\mathbf{m},\alpha}\, \hat\rho_{-\mathbf{m},\gamma}\, \beta\tilde w_{\alpha\gamma}(\mathbf{k_m}).\qquad(22)$$

Calculating F_{ex} in reciprocal space allows one to replace the double spatial integration in Eq. (1) by a single summation over $\mathbf{m}$. Moreover, we note that the evaluation of $\rho_{\mathbf{n},\alpha}$ and $\hat\rho_{\mathbf{m},\alpha}$ does not require *per se* any knowledge of the specific

kind of Bravais lattice, as shown by Eqs. (20) and (21). The information concerning the lattice enters in Eq. (22) *only* via the vectors $\mathbf{k_m}$ at which $\tilde{w}_{\alpha\gamma}$ is determined. This feature can be usefully exploited by performing the optimization of ω_D not only with respect to $\rho_{\mathbf{n},\alpha}$ but also to the vectors $\mathbf{a}_i$ of the unit cell, along the lines laid out by Parrinello and Rahman[31] in the context of molecular dynamics simulation. In a fully numerical implementation of DFT like that considered here, the most straightforward minimization method would consist in discretizing the density profile $\rho_\alpha(\mathbf{r})$ in a box assumed to be large enough to contain many primitive cells and minimizing only with respect to the discrete values of $\rho_\alpha(\mathbf{r})$. However, in doing so, the size of the box will not, in general, be commensurate with the intrinsic periodicity of the lattice which the particles are expected to form at equilibrium. This may lead to the formation of metastable states or periodic structures whose free energy is artificially higher than that of the unconstrained system.

The problem was in fact clearly acknowledged in previous investigations and addressed by making adjustments in the length of the box edges, performing a separate minimization for each of them and selecting the choice which would give the optimal free energy. This procedure was applied to pattern formation in systems with competing interactions in two[7] and three[42] dimensions, but in the latter case, the density profile was assumed to vary only along one direction. An algorithm implementing a similar method was also used in SCFT calculations of the structures formed by hard dumbbells with attractive interactions in two dimensions.[37] For the more general case of a density profile which may vary in three directions, we reckon that such a procedure would prove to be very cumbersome, because of the computer time required by a single minimization run and the increased dimensionality of the parameter space where the search should be made. The method adopted here circumvents these difficulties by assuming from the outset that the density profile consists of periodic replicas of the same unit cell over the whole space and including the cell axes among the quantities to be optimized on the same footing as the values of $\rho_{\mathbf{n},\alpha}$ inside the cell rather than varying them *a posteriori*. The only constraint that we have introduced in this respect is the assumption that the vectors $\mathbf{a}_i$ which define the unit cell are mutually orthogonal. As a consequence, the matrix $\mathbf{A}$ can be written in diagonal form and we have

$$\mathbf{k_m} = (h_1 m_1, h_2 m_2, h_3 m_3), \tag{23}$$

$$\mathbf{R_l} = \left(\frac{2\pi}{h_1} l_1, \frac{2\pi}{h_2} l_2, \frac{2\pi}{h_3} l_3\right), \tag{24}$$

where h_i denote the eigenvalues of $2\pi\mathbf{A}^{-1}$.

The numerical minimization of ω_D has been performed by a preconditioned conjugate-gradient algorithm with adaptive step-size, which can be regarded as a refinement of the basic steepest descent.[29] The latter consists in updating recursively $\rho_{\mathbf{n},\alpha}$ and h_i by moving "downhill" in the direction opposite to the gradient of the function to be minimized, until convergence up to a prescribed accuracy is obtained,

$$\rho_{\mathbf{n},\alpha}^{k+1} = \rho_{\mathbf{n},\alpha}^k - \eta \left.\frac{\partial\beta\omega_D}{\partial\rho_{\mathbf{n},\alpha}}\right|_k, \tag{25}$$

$$h_i^{k+1} = h_i^k - \delta \left.\frac{\partial\beta\omega_D}{\partial h_i}\right|_k, \tag{26}$$

where k and $k+1$ denote, respectively, the starting and updated quantities at the kth iteration, and the parameters η and δ determine the width of the downhill step. The details of the method are illustrated in the Appendix. The density profile inside the cell was sampled at $2^7 \times 2^7 \times 2^7 = 2\,097\,152$ points. The discrete three-dimensional Fourier transforms were calculated by the FFTW package.[43] The lengths of the cell axes in direct space were initially set at $2\pi/h_i = 10R_{11}$ and then left free to evolve according to Eq. (26).

It should be stressed that, since ω_D is not globally convex, it admits in general many local minima for a given thermodynamic state. In fact, this situation is typical of systems with soft repulsive interactions. It has been shown that these systems may exhibit many different crystal structures, including rather exotic ones.[44–47] Therefore, the problem of finding the most stable structure for a certain thermodynamic state arises. Here, we have adopted a naive approach, consisting in performing many ($\gtrsim 30$) runs for each state, corresponding to different minimization paths. Specifically, the trial density profile was set either to a uniform value with a superimposed random noise for different random sequences, or to a sinusoidal modulation with different periods, or to a local minimum of a nearby state. Different switching frequencies from conjugate gradients to steepest descent were used (see the Appendix), performing one steepest descent step every 10 or 50 conjugate gradient iterations or sticking to the steepest descent for the whole run. Finally, in some runs, both the densities $\rho_{\mathbf{n},\alpha}$ and the axis lengths in reciprocal space h_i were perturbed by superimposing to them a random noise every 20 or 50 iterations, and the difference $\Delta\omega_D$ between the grand potential per unit volume of the perturbed and unperturbed states was determined. The perturbed state was always accepted for $\Delta\omega_D < 0$ and accepted with probability $\exp(-\beta\Delta\omega_D)$ for $\Delta\omega_D > 0$.

Of course, for a given thermodynamic state, some (possibly most) of the paths thus generated would converge to the same minimum. In this respect, it should be noted that, while the method described above is based on the periodicity of the density profile $\rho_\alpha(\mathbf{x})$, so that $\rho_\alpha(\mathbf{x})$ in the continuum is obtained by replicating over $\mathbb{R}^3$ the cell in which it is sampled, nothing prevents this cell from consisting of an integer number of primitive cells of the Bravais lattice, rather than coinciding with a primitive cell itself. On the one hand, this feature allows to include in our search also some Bravais lattices whose primitive vectors are not orthogonal, like the triangular one. On the other hand, for a given thermodynamic state, one may find convergence to the same kind of lattice and yet to cells of different sizes, e.g., if the trial density profile used to start the minimization is changed. Whenever this happens, the density profile, the underlying Bravais lattice, and the free energy per unit volume are rigorously the same, as it should be given that these solutions represent the same physical state. This can be taken as a test of the numerical accuracy of the algorithm. Nonetheless, the fact that the same local minimum is obtained many times as $\rho_\alpha(\mathbf{x})$ is sampled in different unit cells negatively affects the efficiency of the search of the absolute minimum. Limiting these instances of multiple

convergence to the same state is in fact the main reason why the angles between the cell axes were not included in the minimization. Several checks in which the angles were also allowed to change have been performed, but only *a posteriori*, in order to test the stability of the structures obtained by assuming orthogonal axes, see Sec. V B.

Despite the relative inefficiency of our brute-force search, many different structures were indeed obtained. For given chemical potentials μ_1 and μ_2 of the two species, the structure corresponding to the minimum value of ω_D was identified as the most stable one. In previous works, the optimal crystal lattices of other soft repulsive potentials were identified by means of a sophisticated genetic algorithm.[45–47] This requires that the information on the lattice is encoded in a "chromosome" containing a relatively small number of "genes." Therefore, it cannot be applied directly to the minimization as formulated here, given that it involves not only the cell axes but also the values of the density at $\sim 10^6$ points. Some hybrid scheme might in principle be considered, where the genetic part of the algorithm acts only on the cell axes, or is employed to generate zero-temperature configurations, which are then fed into the finite-temperature minimization as trial density profiles. Alternatively, other minimization methods tailored to problems with many local minima have been proposed,[48] e.g., basin hopping or minima hopping techniques, which have been successfully applied to the prediction of the structure of Lennard-Jones clusters.[49,50] However, in order to take advantage of these or other sophisticated minimization methods within the present algorithm, its speed of convergence to a local minimum should almost surely be much faster than it actually is.

III. GENERALIZED EXPONENTIAL MODEL

Before considering the Gaussian mixture, it is useful to test the reliability of the algorithm presented here by applying it to a system for which extensive results are already available. To this end, we turn to the generalized exponential model of exponent 4 (GEM-4), which has been studied thoroughly by both DFT and simulations.[11,12] This consists of a one-component fluid of soft particles interacting via the potential

$$w(r) = \epsilon \exp[-(r/R)^4]. \tag{27}$$

In the following, reduced temperatures $T^* \equiv k_B T/\epsilon$ and densities $\rho^* \equiv \bar{\rho} R^3$ will be used.

The GEM-4 belongs to the $Q^{\pm}$ class of potentials[14] mentioned above, i.e., its Fourier transform has a negative minimum at $k \neq 0$. This leads to cluster formation also in the one-component system, at variance with the Gaussian potential. Previous DFT results[11,12] for the GEM-4 potential were obtained by using the free-energy functional $\beta F = \beta \Omega + \beta \mu \int d^3 \mathbf{r} \rho(\mathbf{r})$, where $\beta \Omega$ is grand potential functional (1) specialized to the one-component case. Hence, the functional is the same as that used here, save for the fact that here the calculations have been performed in the grand canonical ensemble, while in Refs. 11 and 12, the canonical ensemble was used. The only difference concerns the functional minimization that here has been performed by the method described in Sec. II B or rather its particularization to a one-component fluid. In
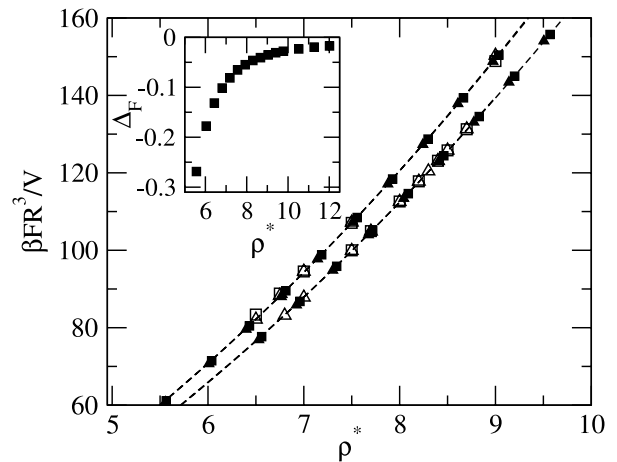

FIG. 1. Reduced Helmholtz free energy density $\beta F R^3/V$ of the GEM-4 model as a function of the reduced density ρ^* at constant temperature $T^* = 1$ (upper curve) and $T^* = 1.1$ (lower curve). Filled symbols refer to the present DFT calculation and open symbols to the Monte Carlo results of Ref. 11. In both cases, triangles correspond to the bcc lattice and squares to the fcc lattice. The dashed lines represent the DFT calculation of Ref. 11 based on the Gaussian parameterization of the density profile; bcc and fcc lattices are undistinguishable on the scale of the figure. A thermodynamically irrelevant chemical-potential shift $\rho^*/(2T^*)$ has been subtracted to our DFT results in order to match the definition of Ref. 11. The inset shows the difference Δ_F between the DFT free energy density obtained by the present calculation and that obtained by the Gaussian parameterization for the fcc phase at $T^* = 1$.

Refs. 11 and 12, the density profile was instead assumed to consist of a superposition of Gaussians centered at the sites of a specified Bravais lattice, taking the lattice spacing and the width of the Gaussians as variational parameters. This led to the prediction of body-centered cubic (bcc) and face-centered cubic (fcc) cluster phases, and in both cases, the Helmholtz free energies were found to be in excellent agreement with Monte Carlo simulations.[11]

These results are compared with the predictions of our DFT calculations in Fig. 1 for several densities and two temperatures $T^* = 1$ and $T^* = 1.1$. Our data for the Helmholtz free energy fall squarely on the curves drawn by the DFT with Gaussian parameterization of the density profile, which in turn are undistinguishable from the simulation results (note that in our grand canonical calculation, the densities are obtained *a posteriori* and do not coincide with those of the simulations). As a matter of fact, the agreement between the two DFT approaches is so close that on the scale of the figure, one cannot even tell whether the unconstrained minimization leads to a lower free energy, as it should. To this end, in the inset, we have plotted the difference Δ_F between $\beta F/V$ at $T^* = 1$ given by the unconstrained minimization and the same quantity given by the Gaussian parameterization, which is indeed everywhere negative. At the same time, the extent of the relative deviation is very small, and becomes more and more so as ρ increases, because of both the decrease of $|\Delta_F|$ and the increase of $\beta F/V$. On the one hand, this shows the accuracy of the minimization algorithm used here. On the other hand, for this system, the simpler Gaussian parameterization already yields very accurate results, and there is little reason for going beyond it.

Figure 2 shows the density profile $\rho^*(\mathbf{r})$ along the line connecting nearest-neighbor sites for the bcc lattice at $T^* = 1$ and $\rho^* = 6.40$ and the fcc lattice at $T^* = 1$ and $\rho^* = 8.30$.
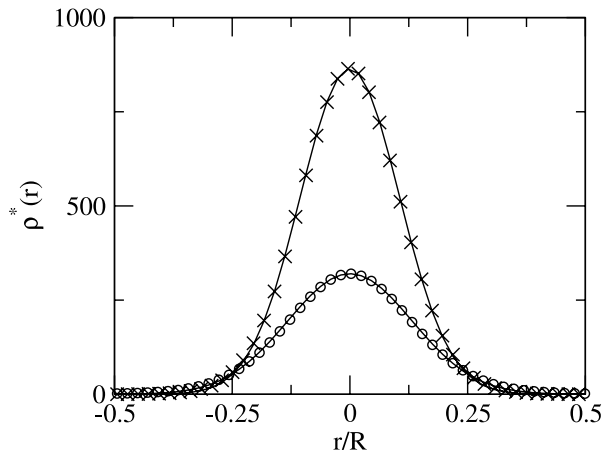
FIG. 2. Reduced density profile $\rho^*(\mathbf{r})$ in the neighborhood of the peak along the line connecting nearest-neighbor sites. Circles: $T^* = 1$, $\rho^* = 6.40$, and bcc lattice. Crosses: $T^* = 1$, $\rho^* = 8.30$, and fcc lattice. Solid lines: Gaussian fit of the above data.

In both cases, the peak of $\rho^*(\mathbf{r})$ is indeed undistinguishable from its representation as a Gaussian with suitably chosen amplitudes and widths, also shown in the figure. In fact, the Gaussian shape of the peak was already established in Ref. 11 by inspection of the density profile obtained by simulations. Some deviations of $\rho(\mathbf{r})$ from its Gaussian representation can be detected by moving out of the very neighborhood of the peak and focusing on the tail region, which cannot be resolved accurately on the scale of Fig. 2. To this end, in Fig. 3, we have plotted the logarithm of $\rho(\mathbf{r})$ for the same states and along the same direction as those considered in Fig. 2 as a function of r^2, so that a Gaussian would give a straight line. The figure also shows the results obtained by representing $\rho(\mathbf{r})$ as a superposition of Gaussians centered at the lattice sites and identical to those of Fig. 2, whose amplitude and width have been determined by a best fit to $\rho(\mathbf{r})$ in the peak region. It is clear that the tail of $\rho(\mathbf{r})$ is non-Gaussian: specifically, $\rho(\mathbf{r})$ decays more slowly than its Gaussian representation. Hence, although still strongly localized at the lattice sites, in the region between two peaks, the density profile is larger than what
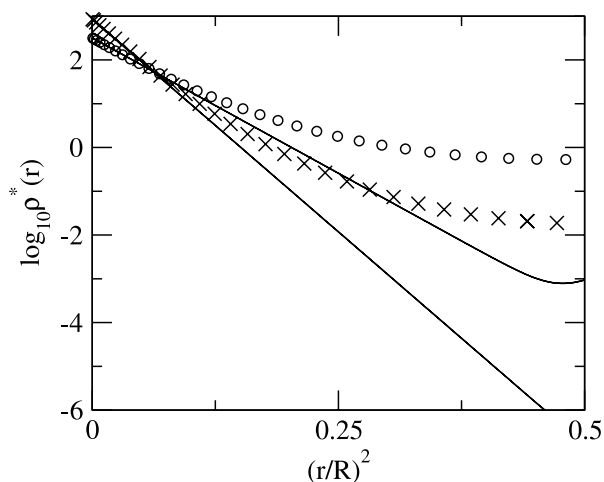

FIG. 3. Logarithm of $\rho^*(\mathbf{r})$ along the line connecting nearest-neighbor sites as a function of r^2. Symbols as in Fig. 2. The solid lines refer to the representation of $\rho(\mathbf{r})$ as a sum of Gaussians centered at the lattice sites.
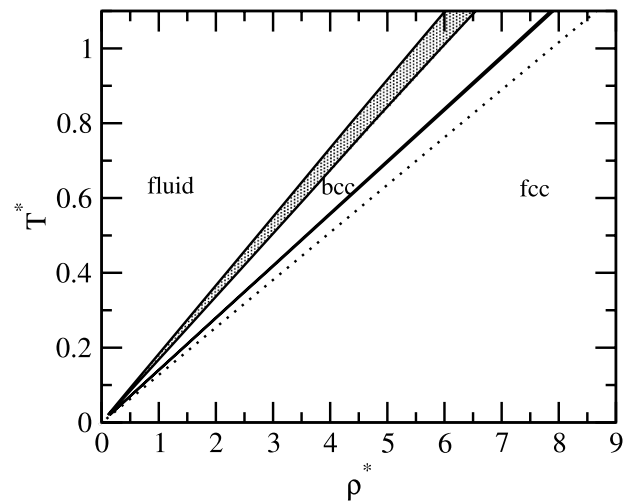

FIG. 4. Phase diagram of the GEM-4 model in the T^*-ρ^* plane. The grey domain is the fluid-bcc coexistence region and the thin black domain is the bcc-fcc coexistence region. The dotted line is the λ-line.

could be inferred by representing each peak as a Gaussian. Nevertheless, as remarked above, the thermodynamics is not appreciably affected by this rather fine-structure details.

The phase diagram of the GEM-4 model in the T^*-ρ^* plane predicted by the present approach is plotted in Fig. 4. The thermodynamic quantities of the fluid phase have been obtained by evaluating grand potential functional (1), or rather its one-component analogue, for a uniform state $\rho(\mathbf{r}) \equiv \bar{\rho}$. This corresponds to the RPA compressibility route, whose chemical potential is given by one-component analogue of Eq. (2). As the density is increased, two first-order transitions are found: one from the homogeneous fluid to the bcc phase and another one at higher density from the bcc to the fcc phase. The coexistence region between the bcc and fcc phases agrees very closely with that shown in Fig. 1 of Ref. 11 and, again as in Ref. 11, is much narrower than that between the fluid and bcc phases. For the system considered here, the λ-line in the ρ-T plane is a straight line,[11,12] which lies strictly inside the domain where the solid phases are thermodynamically stable, similarly to the spinodal line for liquid-vapor equilibrium.

It is worthwhile observing that in Ref. 11, the properties of the fluid were determined by the RPA energy route, rather than the compressibility route used here. This determines the only difference between the two phase diagrams, which concerns the topology of fluid-solid equilibrium. The fluid-solid coexistence region found in Ref. 11 is wider than that obtained here and shifted to slightly higher densities, especially on the solid side. As a consequence, it intersects the bcc-fcc coexistence region at a triple-point temperature $T_t^* \simeq 0.4$, at which the fluid, bcc, and fcc phases coexist at equilibrium. At temperatures below T_t, the bcc phase is no longer present, and coexistence is between fluid and fcc phases. Here, on the other hand, there is no triple point and the bcc region gets narrower and narrower as the temperature is reduced, but persists down to $T = 0$. We remark that this difference, although *per se* significant, is due to the different results for the free energy of the fluid phase because of the thermodynamic inconsistency of the RPA: when solid-solid equilibrium is considered, the predictions of the two DFT approaches are hardly distinguishable.

For the sake of completeness, we may also recall that the existence of a fluid-bcc-fcc triple point in the phase diagram of the GEM-4 potential has been confirmed by numerical simulation, but at a much lower temperature than the above-mentioned value $T_t^* \simeq 0.4$. In fact, the simulation phase diagram reported in Ref. 13 did not show a triple point down to $T^* = 0.2$, and subsequent simulations[51] located it at $T_t^* = 0.078$ and $\rho^* \simeq 0.9$. The large discrepancy with respect to the DFT prediction was ascribed in Ref. 13 to a deterioration of the performance of DFT in the low-density, low-temperature region combined with the sensitivity of the position of the triple point to small changes in the slopes of the fluid-bcc and bcc-fcc coexistence curves.

The features of cluster formation in the GEM-4 and, more generally, in $Q^{\pm}$ potentials are well understood and have been thoroughly described.[11,12] In order to compare them with the behavior of the Gaussian mixture considered in Sec. V C, in Fig. 5, we have reported the number of particles per cluster n_c, the distance between nearest-neighbor clusters d, and the width of the density peaks obtained by a fit to a Gaussian of variance σ, for the fcc phase at $T^* = 0.4$. We have chosen the fcc phase over the bcc since it allows to explore a wider density interval. As shown in panel (a), the lattice constant is basically independent of density, in stark contrast with the behavior of atomic crystals. This is due to the negative minimum of the Fourier transform of the interaction at a non-vanishing, density-independent wave vector k_λ, which strongly favors

density modulations with characteristic length $\sim 2\pi/k_\lambda$. The figure also shows the estimate $d \simeq d_\lambda = \pi\sqrt{6}/k_\lambda$ obtained by identifying k_λ with the nearest-neighbor distance in reciprocal space.

Since d is nearly constant, increasing the density ρ must necessarily result in an increase of n_c. The latter must be a linear function of ρ according to the relation[12]

$$n_c = \gamma\, d^3 \rho, \qquad (28)$$

where γ is a lattice-dependent coefficient. The dependence of n_c on ρ is illustrated in panel (b), which displays the results for n_c obtained as the ratio between the average number of particles and the number of density peaks in the unit cell. These have been compared with the above linear expression by fixing d at its value at the point at lowest density among those in the figure, $\rho^* \simeq 3.24$, and γ at the value $\sqrt{2}/2$ of the fcc lattice. Setting $d = d_\lambda$ would actually give the bcc lattice with $\gamma = 4\sqrt{3}/9$ as the most stable structure.[12] The linear dependence thus obtained has also been plotted in the figure. The three plots nearly fall on the top of one another, showing that n_c is indeed an almost perfectly linear function of ρ.

Finally, panel (c) reports the localization parameter of the density peaks, obtained by fitting each peak to a Gaussian of variance σ. Not surprisingly, as the density decreases, the peaks become less localized. Nevertheless, the degree of localization remains relatively high even at the lowest density of the figure, at which σ is still about one order of magnitude smaller than the characteristic size R of the particles. Hence, the preference of the system for a specific value of the lattice constant d is so strong that not only do clusters form a distance d apart from each other but also particles within a certain cluster are almost completely superimposed. The inset of panel (c) shows the Lindemann ratio L, defined as the root mean square displacement $\sqrt{3}\sigma$ of a particle divided by the nearest-neighbor distance d. The values of L are appreciably smaller than the estimate $L \simeq 0.189$ obtained in Ref. 12, but one should keep in mind that the latter result refers to the behavior of L at freezing, while the states considered here lie in the fcc region of the phase diagram, so that their densities are higher than the density of the melting line which, in turn, is higher than the density of the approximate freezing line of Ref. 12. At the same time, the observation made in that study, that cluster crystals are able to support values of L significantly larger than those characteristic of atomic crystals, holds also for the present situation. In fact, according to the empirical Lindemann criterion, an atomic solid is expected to melt for $L \simeq 0.1$, while clearly this is not the case for the states displayed here, none of which is close to the melting line, despite the fact that their L is slightly above or slightly below 0.1.

We conclude this section by recalling an interesting feature of the phase diagram of the GEM-4 potential at low temperature which is completely missed by the DFT treatment considered here, namely, the presence of a sequence or "cascade" of isostructural transitions between different fcc phases, ending at a sequence of critical points. This was first pointed out in Ref. 52 and then confirmed by simulation in Refs. 51, 53, and 54. As explained in Ref. 52, such a behavior is due to the fact that at zero temperature, the number of particles in a cluster n_c is bound to assume integer values, and this
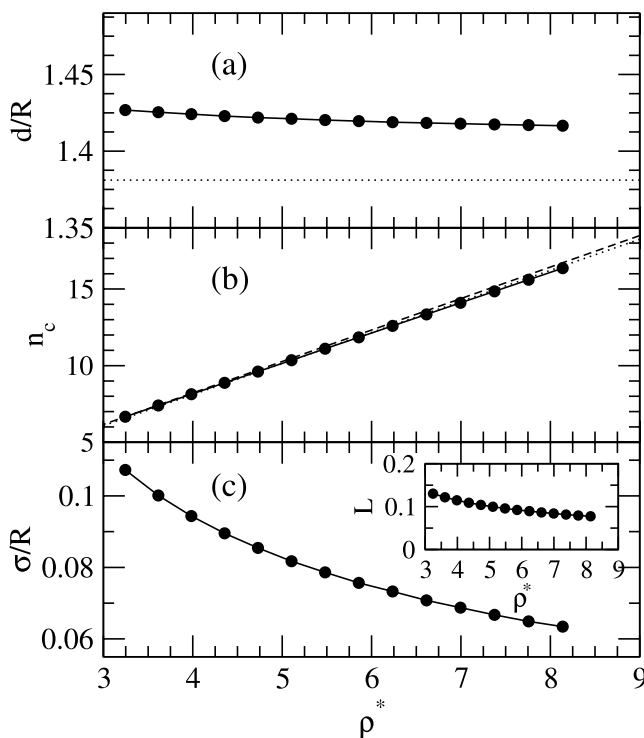

FIG. 5. Distance between nearest-neighbor clusters d (panel (a)), number of particles per cluster n_c (panel (b)), and localization parameter σ (panel (c)) for the fcc phase of the GEM-4 potential at $T^* = 0.4$. The inset of panel (c) is the Lindemann ratio $\sqrt{3}\sigma/d$. The filled points are the results of numerical minimization of functional (1). Solid lines are a guide for the eye. The dotted lines in panels (a) and (b) are the results for d and n_c obtained by setting the nearest-neighbor distance in reciprocal space at the wave vector k_λ of the λ-line (see text). The dashed line in panel (b) is the result for n_c obtained by fixing d at its value at the point at lowest density among those in the figure.

entails a corresponding discretization of the lattice constant, which persists up to non-vanishing, albeit low temperatures, $T^* \lesssim 0.05$. Mean-field functional (1), on the other hand, does not incorporate the correlations which prevent the particles from freely redistributing among the lattice sites at low T and as a consequence does not give a discretization of n_c at any temperature.[52] We remark that this feature is intrinsic to the mean-field nature of the functional, irrespective of whether the density profile is represented as a superposition of Gaussians as in Refs. 11 and 12 or its form is left unconstrained as in the present treatment.

Determining a functional in which these correlation effects are taken into account is a very interesting issue,[55] but is clearly out of the scope of the present paper. The GEM-4 potential has been considered here simply as a test bed of the minimization algorithm presented in Sec. II B rather than that of free-energy functional (1). Hence, we have focused on relatively high temperatures, where this functional is already known to be very accurate. In this regime, the numerical DFT minimization used here reproduces the expected results for the free energy and phase diagram of the GEM-4 model, although for this particular interaction, there is little need to go beyond the Gaussian parameterization of the density profile employed in previous investigations.[11,12]

IV. OCCURRENCE OF MICROPHASES IN GAUSSIAN MIXTURES

We now come to the Gaussian mixture, which is the main topic of this study. For this system, the pair potential $w_{\alpha\gamma}(r)$ reads

$$\beta w_{\alpha\gamma}(r) = \epsilon_{\alpha\gamma} \exp[-(r/R_{\alpha\gamma})^2], \tag{29}$$

where $\epsilon_{\alpha\gamma} > 0$ and $R_{\alpha\gamma} > 0$ determine the interaction strengths and ranges, respectively. The above potential provides a simple modelization of the effective interactions between polymer chains in an athermal solvent. For chains of species α, one has[17,18] $\epsilon_{\alpha\alpha} \simeq 2$, while $R_{\alpha\alpha}$ is proportional to the gyration radius of the polymer. We remark that, unlike the GEM-4 potential considered in Sec. III, here $\beta w_{\alpha\gamma}(r)$ is athermal because of the entropic origin of the interactions, so that the temperature is not a relevant thermodynamic variable.

Most investigations of the phase diagram of binary Gaussian mixtures were focused on the spinodal instability and the ensuing demixing transition.[21–23,56] In Ref. 21, it was shown that, within the RPA, the spinodal line exists provided the interaction parameters $\epsilon_{\alpha\gamma}$ and $R_{\alpha\gamma}$ satisfy the condition

$$\left(\frac{R_{11}R_{22}}{R_{12}^2}\right)^3 < \frac{\epsilon_{12}^2}{\epsilon_{11}\epsilon_{22}}. \tag{30}$$

As discussed in Ref. 22, specifying the interaction strengths in such a way that $\epsilon_{12} < \epsilon_{11} \simeq \epsilon_{22}$, which is an appropriate choice to model polymer mixtures,[17] tends to make demixing energetically unfavorable. Nevertheless, Eq. (30) shows that demixing may still take place, provided R_{12} is large enough. If this is the case, the relatively long range of the repulsion between unlike species will compensate for its small strength, and particles of different species will be driven away from one another. This

situation is favored by positive non-additivity of the interaction ranges, such that $R_{12} > (R_{11} + R_{22})/2$. In Refs. 21–23, the demixing transition was studied by setting the interaction parameters at $\epsilon_{11} = \epsilon_{22} = 2$, $\epsilon_{12} = 1.888$, $R_{22} = 0.665R_{11}$, and $R_{12} = 0.849R_{11}$, where R_{11} sets the length unit in the problem. This value of R_{12} was determined by the relation[17]

$$R_{12}^2 = \frac{1}{2}(R_{11}^2 + R_{22}^2), \tag{31}$$

which indeed implies positive non-additivity.

According to the above line of reasoning, one expects that the effect of *negative* non-additivity is to inhibit demixing, since in this case, both the strength and the range of the interactions favor those configurations in which particles of different species are neighbors. Hence, negative non-additivity may seem at first less interesting than positive non-additivity as far as phase behavior is concerned. However, in Ref. 20, it was pointed out that, for high enough negative non-additivity, the affinity between particles of different species is so strong that not only is demixing inhibited but the mixture can also form ordered structures in order to take maximum advantage from such an affinity. By taking $\epsilon_{11} = \epsilon_{22} = 2$, $\epsilon_{12} = 1.888$, and $R_{22} = 0.665R_{11}$ as above and decreasing R_{12} to $R_{12} = 0.6R_{11}$, it was shown that the spinodal is replaced by a λ-line and that inside the region bounded by λ-line ordered, crystal-like phases with multiple occupancy of the lattice sites are thermodynamically favored with respect to the homogeneous phase. The above set of interaction parameters will be adopted here as well for the detailed study of the phase diagram but, before doing so, it may be worthwhile considering more in general which conditions on these parameters lead to a λ-line.

Equation (9) is equivalent to a divergence at $k \neq 0$ of the partial structure factors $S_{\alpha\gamma}(k)$ or, equivalently, of the pair correlation functions $\tilde{h}_{\alpha\gamma}(k)$ in Fourier space. If Eq. (6) is used for the direct correlation functions together with the Ornstein-Zernike (OZ) equation for a binary fluid, one obtains

$$\tilde{h}_{11}(k) = -\frac{\varphi_{11}(k) + \bar{\rho}_2[\varphi_{11}(k)\varphi_{22}(k) - \varphi_{12}^2(k)]}{[1 + \bar{\rho}_1\varphi_{11}(k)][1 + \bar{\rho}_2\varphi_{22}(k)] - \bar{\rho}_1\bar{\rho}_2\varphi_{12}^2(k)}, \tag{32}$$

$$\tilde{h}_{12}(k) = -\frac{\varphi_{12}(k)}{[1 + \bar{\rho}_1\varphi_{11}(k)][1 + \bar{\rho}_2\varphi_{22}(k)] - \bar{\rho}_1\bar{\rho}_2\varphi_{12}^2(k)}, \tag{33}$$

where $\varphi_{\alpha\gamma}(k)$ is a short-hand notation for $\beta\tilde{w}_{\alpha\gamma}(k)$, and the denominator in the rhs is just $\bar{\rho}_1\bar{\rho}_2 \det \|\tilde{c}_{\alpha\gamma}(k)\|$. For Gaussian potential (29), one has

$$\beta\tilde{w}_{\alpha\gamma}(k) = \pi^{3/2}R_{\alpha\gamma}^3\epsilon_{\alpha\gamma} \exp[-(R_{\alpha\gamma}k)^2/4]. \tag{34}$$

The expression of $\tilde{h}_{22}(k)$ is obtained by swapping the indexes 1 and 2 in Eq. (32). Equation (32) can be used to obtain the effective pair potential $w_{11}^{\text{eff}}(r)$ between particles of species 1 in the mixture. Within RPA, the effective interaction w_{11}^{eff} coincides with the low-density limit $\bar{\rho}_1 \to 0$ of the correlation function, thereby yielding

$$\beta\tilde{w}_{11}^{\text{eff}}(k) = \varphi_{11}(k) - \frac{\bar{\rho}_2\varphi_{12}^2(k)}{1 + \bar{\rho}_2\varphi_{22}(k)}, \tag{35}$$

as well as the corresponding expression for $\beta\tilde{w}_{22}(k)$ by swapping the indexes in Eq. (35). This can be checked by replacing the binary mixture with the one-component fluid of particles 1

interacting via the effective potential $w_{11}^{\mathrm{eff}}(r)$ and using again RPA together with the OZ equation to obtain its pair correlation function $h_{11}^{\mathrm{eff}}(r)$ via the relation

$$\tilde{h}_{11}^{\mathrm{eff}}(k) = -\frac{\beta \tilde{w}_{11}^{\mathrm{eff}}(k)}{1 + \bar{\rho}_1 \beta \tilde{w}_{11}^{\mathrm{eff}}(k)}. \tag{36}$$

If $\tilde{w}_{11}^{\mathrm{eff}}(k)$ as given by Eq. (35) is substituted in Eq. (36), one indeed finds that $\tilde{h}_{11}^{\mathrm{eff}}(k)$ gives back the expression of $\tilde{h}_{11}(k)$ of Eq. (32). In other words, *within RPA*, effective potential (35) fully accounts for the effect of particles of species 2 on the correlations between particles of species 1: there is no loss of information due to disregarding many-body contributions to the effective interaction. By the same token, this remains true if one focuses on the effect of particles 1 on the correlations between particles 2, i.e., the RPA correlations are recovered irrespective of whether the effective interaction considered is that between the larger particles mediated by the smaller ones or that between the smaller particles mediated by the larger ones.

Before going any further, we should make two observations regarding the above property: First, it rests on the soft-core character of the interactions, which allows one to identify the perturbation in the RPA with the total potential, thereby obtaining Eq. (6) for the direct correlation functions. Second, it may actually point at a deficiency, rather than a strength, of the RPA: the ability of Eq. (35) to recover completely the correlations between particles of species 1 is due to the very simple form of the RPA correlations, such that the many-body effects which would make $h_{11}^{\mathrm{eff}}(r)$ different from $h_{11}(r)$ may not be there in the first place. It is known that this simple form is actually sufficient to describe the correct behavior of the correlations between soft-core particles in the high-density limit,[21] in which mutual particle overlaps lead to weaker and weaker correlations, and RPA becomes exact. However, this may no longer be the case at lower density. In Ref. 56, a thorough DFT study of the effective interactions in Gaussian mixtures was carried out based on the test-particle method, in which functional (1) and its generalization to multicomponent mixtures were employed to obtain the density profile of, say, particles of species 2 around a single particle of species 1, and the result was then used to determine the effective 1-1 pair interactions as the work necessary to bring a particle 1 at a given distance from another particle of the same species. One of the conclusions of that study is that, as a consequence of the approximations inherent to the RPA, the effective potential thus obtained can be very different from that obtained via the OZ equation for $h_{11}(r)$ and that there are strong reasons to believe that in such an instance, the test-particle method is that which gives the more reliable results.

Notwithstanding these concerns, we should keep in mind that, as long as one is interested in the existence and position of the λ-line, the RPA and the test-particle routes to the correlations are equivalent, because they give *the same* poles for $\tilde{h}_{ij}(k)$,[56] namely, the roots of the denominator of Eqs. (32) and (33). Moreover, according to the above analysis, the existence of the λ-line is equivalent to a divergence at $k \neq 0$ of the structure factor $S(k)$ of the one-component fluid interacting via $w_{11}^{\mathrm{eff}}(r)$. Hence, to the extent to which the former occurrence

can be trusted as an indication of microphase formation, the latter can be equally trusted. We then turn to the behavior of the one-component system.

In Eq. (35), the first term in the rhs is clearly the bare Gaussian interaction between particles 1, while the second term represents the attractive contribution of the depletion forces exerted on particles 1 by particles 2, screened by the interaction between particles 2 themselves. This contribution may lead to bulk phase separation, but also to clustering and microphases. As stated in Sec. I, in order for a one-component fluid to support cluster formation, its pair potential must belong to the $Q^\pm$ class.[14] It is straightforward to see that $w_{11}^{\mathrm{eff}}(r)$ can belong to this class, even though the Gaussian potential $w_{11}(r)$ does not. If we assume that $\tilde{w}_{11}^{\mathrm{eff}}(k = 0)$ is positive, which is always the case provided $\bar{\rho}_2$ is chosen suitably small, then a *sufficient* condition for this to happen is

$$R_{11} > \sqrt{2} R_{12}. \tag{37}$$

If this condition is satisfied, $\tilde{w}_{11}^{\mathrm{eff}}(k)$ goes to zero from negative values at large k, so it must have a negative minimum at some non-vanishing $k = k_\lambda$. Equation (36) then implies a divergence of $S_{11}(k)$ at k_λ for large enough $\bar{\rho}_1$. According to the analysis carried out above, this is equivalent to the denominator of Eqs. (32) and (33) vanishing at k_λ, which implies that $S_{22}(k)$ diverges at k_λ as well. By virtue of Eq. (36), this in turn implies that also $\tilde{w}_{22}^{\mathrm{eff}}(k)$ has a negative minimum at k_λ, i.e., also $w_{22}^{\mathrm{eff}}(r)$ belongs to the $Q^\pm$ class. Hence, in order to obtain a λ-line, it is sufficient that Eq. (37) is fulfilled by only one of the two species. As just stated, Eq. (37) is a sufficient condition for the effective interactions to belong to the $Q^\pm$ class, not a necessary one. For instance, the choice of interaction parameters corresponding to "system B" in Ref. 24, in which binary Gaussian mixtures appropriate to model dendrimer solutions were considered, does not fulfill Eq. (37) and still gives a λ-line. On the other hand, the parameters adopted in Ref. 20 do fulfill Eq. (37), since they satisfy the relation $R_{11} > \sqrt{2} R_{12} > R_{22}$. We also note that Eq. (31), which, as discussed above, implies positive non-additivity and favors demixing, is incompatible with Eq. (37). As for negative non-additivity, while it is not generally required by Eq. (37), it becomes so if the two species are not very different in size: it is readily seen that the additivity of the interaction ranges $R_{12} = (R_{11} + R_{22})/2$ is compatible with Eq. (37) only for $R_{22} < (\sqrt{2} - 1)R_{11} \simeq 0.414 R_{11}$, which is not the case for the interaction parameters of Ref. 20.

By way of example, in Figs. 6 and 7, we have plotted the effective potentials $w_{ii}^{\mathrm{eff}}(r)$ and the radial distribution functions $g_{ii}(r) \equiv h_{ii}(r) + 1$, $i = 1, 2$, of the Gaussian mixture with the interaction parameters considered in Ref. 20 at two different thermodynamic states. From now on, the state will be identified as in Ref. 20 by the concentration of the smaller component $c \equiv \bar{\rho}_2/(\bar{\rho}_1 + \bar{\rho}_2)$ and the total density $\bar{\rho} \equiv \bar{\rho}_1 + \bar{\rho}_2$. The latter will be measured in reduced units $\rho^* \equiv \bar{\rho} R_{11}^3$. Figures 6 and 7 refer to $\rho^* = 10$, $c = 0.2$ and $\rho^* = 10$, $c = 0.6$, respectively. These states lie near the λ-line, on the low- and high-concentration sides with respect to its minimum, see Fig. 8. As shown in the insets, for each state, both $\tilde{w}_{11}^{\mathrm{eff}}(k)$ and $\tilde{w}_{22}^{\mathrm{eff}}(k)$ have indeed a negative minimum at non-vanishing, nearly coincident wave vectors $k \simeq k_\lambda$, which are bound to become exactly coincident on the λ-line. The potential $w_{11}^{\mathrm{eff}}(r)$
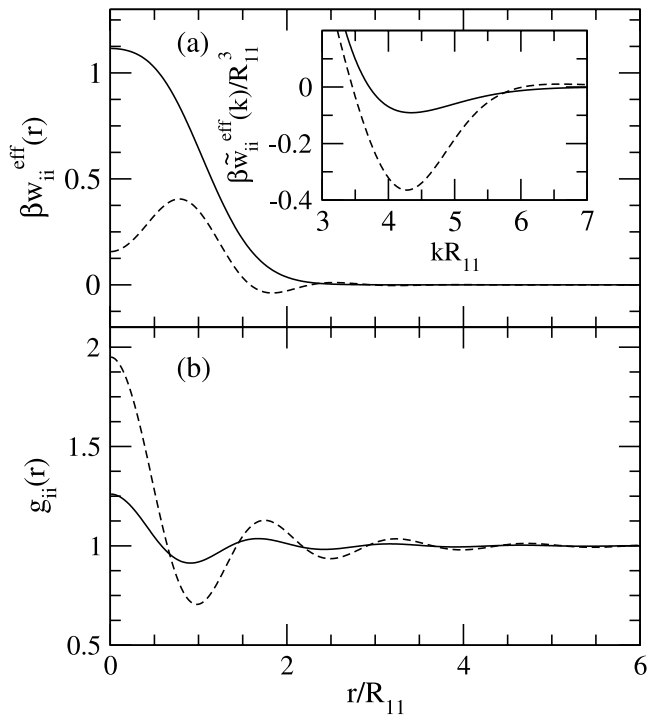
FIG. 6. Effective potentials $w_{ii}^{\mathrm{eff}}(r)$ (panel (a)) and radial distribution functions $g_{ii}(r)$ (panel (b)) of particles of species $i = 1$ (solid line) and $i = 2$ (dashed line) of the binary Gaussian mixture with interaction parameters specified in the text at total density $\rho^* \equiv \bar{\rho} R_{11}^3 = 10$ and concentration $c \equiv \bar{\rho}_2/\bar{\rho} = 0.2$. The inset in panel (a) shows the effective potentials in Fourier space $\tilde{w}_{ii}^{\mathrm{eff}}(k)$ in the neighborhood of the minimum. The expression of $\tilde{w}_{11}^{\mathrm{eff}}(k)$ is given in Eq. (35).

displayed in Fig. 6 resembles the GEM-4[11,12] which has been considered in Sec. III, while the non-monotonic profile of $w_{11}^{\mathrm{eff}}(r)$ in Fig. 7 is similar to that which has been proposed to model effective pair interactions between amphiphilic dendrimers[15,16] and ring polymers.[57]

It is interesting to observe that for both states, the deeper minimum of the effective potential in Fourier space pertains to the less abundant species, i.e., species 2 in Fig. 6 and species 1 in Fig. 7. As a consequence, we expect that this species has a tendency to form bigger density modulations than those of the more abundant species. This is apparent from the radial distribution functions plotted in the lower panels of the figures. At variance with the $g(r)$ of a one-component Gaussian fluid,[21] which has its minimum at $r = 0$ and on increasing r goes to 1 in an essentially monotonic fashion,[56] both $g_{11}(r)$ and $g_{22}(r)$ in Fig. 6 show appreciable oscillations of period $\sim 2\pi/k_\lambda$ and assume their maximum, rather than their minimum, at $r = 0$. Such a behavior is an indication that the mixture tends to form periodic structures in which many particles accumulate in a region comparable with their own size, as in the crystal phases with multiple occupancy studied in Refs. 11 and 12. At the same time, both the amplitude of the oscillations of $g_{ii}(r)$ and its maximum at $r = 0$ are considerably bigger for particles 2 than for particles 1. As a consequence, particles 2 will have a much stronger tendency to arrange into a localized state. This effect is even more evident in the situation illustrated in Fig. 7, in which the less abundant species is that of the larger particles 1. On the one hand, $g_{11}(r)$ is similar to the $g_{22}(r)$ of Fig. 6, thereby showing significant oscillations and a strong
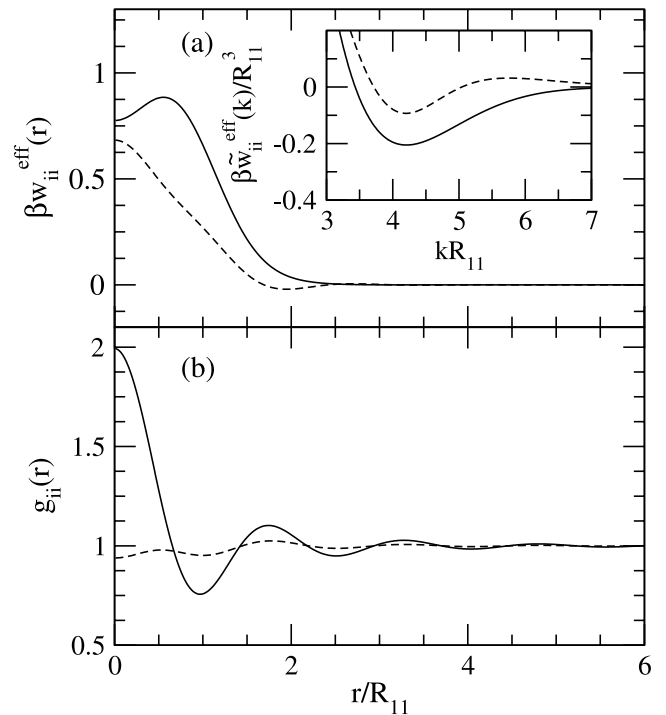
enhancement at $r = 0$. On the other hand, $g_{22}(r)$, unlike the $g_{11}(r)$ of Fig. 6, is relatively structureless and has even a minimum at $r = 0$, although a very shallow one. Hence, the above analysis suggests that, while for certain states the mixture can (and will) form phases which consist of periodic structures of the two species with the same periodicity, the roles played by the two species in such phases may not be necessarily the same: in particular, the species at lower concentration should be more strongly localized than that at higher concentration. Quite interestingly, this is expected to be true not only for a low-concentration arrangement of the larger particles embedded in a matrix of the smaller particles but also for the converse
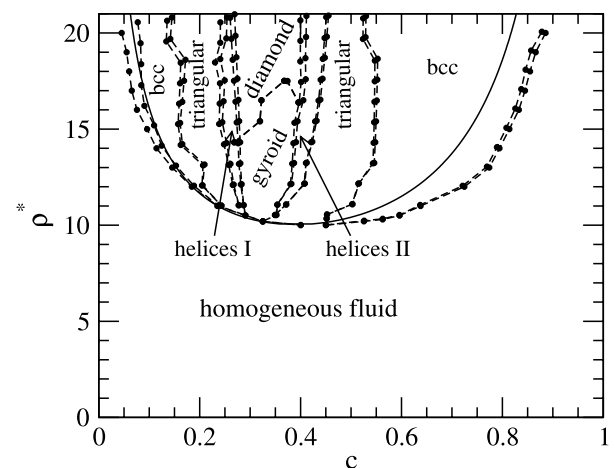

FIG. 7. Same as Fig. 6 for $\rho^* = 10$ and $c = 0.6$.

FIG. 8. Phase diagram of the binary Gaussian mixture with interaction parameters specified in Sec. IV. The quantities ρ^* and c denote, respectively, the total reduced density $\rho^* \equiv \bar{\rho} R_{11}^3$ and the concentration of the smaller component $c \equiv \bar{\rho}_2/\bar{\rho}$. The filled points represent first-order phase boundaries between different phases. The dashed lines are a guide for the eye. The solid line is the λ-line.

situation of a low-concentration arrangement of the smaller particles in a matrix of the larger ones, even though one still expects that localization effects in the matrix will be stronger in the latter case, see the lower panels of Figs. 6 and 7.

These considerations are based on the effective interactions when the λ-line is approached from the outside. The meaning of these interactions lies in the fact that they are able to reproduce the RPA correlations of the binary system which, however, break down inside the region bounded by the λ-line. Hence, they are of little help in obtaining the phase diagram of the mixture. To this end, we will have to turn to the DFT machinery developed in Sec. II B. The results will confirm the qualitative analysis developed here.

V. PHASE PORTRAIT OF A MODEL GAUSSIAN MIXTURE

A. Description of microphases

As stated in Sec. I, the phase diagram has been determined for a model Gaussian mixture with interaction parameters equal to those considered in Ref. 20 and specified in Sec. IV. For this choice, the spinodal line does not exist, but a λ-line is indeed present, i.e., Eqs. (9) and (10) are satisfied for $k \neq 0$ along a locus of the $\bar{\rho}_1$-$\bar{\rho}_2$ plane.

Since the functional minimization was performed in the grand canonical ensemble, $\bar{\rho}$ and c were obtained *a posteriori* as a function of the chemical potentials μ_1 and μ_2 of the two species. As discussed in Sec. II B, in general for given μ_1 and μ_2, a number of different phases were obtained, and the most stable one was identified as that giving the minimum (most negative) value of $\omega_D = -P$. Figure 8 shows the phase diagram thus obtained in the density-concentration plane together with the λ-line. The mixture displays a rather rich behavior with several inhomogeneous phases, which in the figure have been labeled as bcc, triangular, helices I, helices II, gyroid, and diamond. All the boundaries between two distinct phases, say A and B, correspond to first-order transitions and were determined by imposing the conditions of thermodynamic equilibrium $P_A = P_B$, $\mu_1^A = \mu_1^B$, and $\mu_2^A = \mu_2^B$ between the pressures and the chemical potentials of the phases at coexistence. Similarly to what found for the GEM-4 potential in Sec. III, most of the coexistence regions are very narrow, i.e., the coexisting phases have nearly the same densities ρ and concentrations c, except for the fluid-bcc transition at high ρ and low c.

Before considering each of the phases of Fig. 8 in closer detail, we must recall that a tentative phase diagram of the Gaussian mixture in hand based on grand potential functional (1) used here was already proposed by us in an earlier study, see Fig. 5 of Ref. 28. The phase diagram plotted there, however, differs markedly from that presented here. First, we notice that in the former, the boundary between the homogeneous and the inhomogeneous fluid is undistinguishable from the λ-line, whereas in the phase diagram of Fig. 8, the inhomogeneous region is wider than the domain enclosed within the λ-line, especially on the high-concentration side. As recalled in Sec. IV, this situation is akin to that found in the mean-field description of the liquid-vapor transition in a fluid, in which the spinodal line lies strictly inside the

domain bounded by the coexistence curve and occurs also in the clustering transition of $Q^{\pm}$ potentials[11,12] such as the GEM-4 potential considered in Sec. III, notwithstanding the different shape of the λ-line.

Still, the most relevant difference between the phase diagram of Ref. 28 and the present one concerns not so much the size of the inhomogeneous region, as the kind of phases by which it is inhabited. In fact, in Ref. 28, three domains at low, high, and intermediate concentrations were found. The low- and high-concentration domains bear some resemblance to the low- and high-concentration bcc regions shown here, especially at high concentration, where the existence of a bcc phase was also established, while at low concentration, the limited accuracy of our calculation did not allow us to establish whether the most stable phase would be the bcc or the triangular. However, a very different situation is found in the region at intermediate concentration, which in Ref. 28 was assigned to a lamellar or stripe-like phase, such that the density profile $\rho_\alpha(\mathbf{r})$ of each species varies along a single direction, and is then a function of just one scalar variable. This phase does not appear anymore in the present diagram and has been superseded by the host of phases located between the two bcc phases at low and high concentration. The fact that none of them was detected in Ref. 28 has to be traced back to the more naive minimization procedure implemented there, in which $\rho_\alpha(\mathbf{r})$ was not assumed to be periodic and was sampled in a fixed box, with no guarantee that such a box would be commensurate with the periodicity of the lattice for a given thermodynamic state. As observed in Sec. II B as well as in Ref. 28, this may artificially enhance the free energy of some phases or even make them altogether unobservable by replacing them with defective structures, whose occurrence was allowed and were in fact frequently found in that investigation. In this regard, it is perhaps not surprising that the lamellar phase was favored over the other phases, in which the density is modulated along more than one direction, and are then expected to pose stricter commensurability requirements. This problem is made even more relevant by the fact that in the system considered here, as it often happens with microphase formation, different phases can have very similar free energies, so that even a small alteration of their values may significantly affect the phase diagram. Thus, it appears that incorporating the lattice periodicity in the minimization as in the present work is of paramount importance, especially if three-dimensional density modulations are considered.

We observe that, although the mixture studied here is clearly non-symmetric because of the different values of R_{11} and R_{22}, the phase diagram of Fig. 8 displays a symmetry of sorts since, as one moves inside the inhomogeneous domain starting from the homogeneous fluid either on the low- or high-concentration side, one finds in both cases a bcc, a triangular, and a helical phase before reaching the middle region centered at $c \simeq 0.3$. In order to get more insight into the structure of these phases, we will resort to a pictorial representation of the density profiles of the two species $\rho_1(\mathbf{r})$ and $\rho_2(\mathbf{r})$. This is especially useful in the present case in which, as will appear in the following, knowledge of the Bravais lattice alone is not sufficient to describe the particle arrangement. Figures 9-19 have been produced by the VESTA software.[58] From here on,
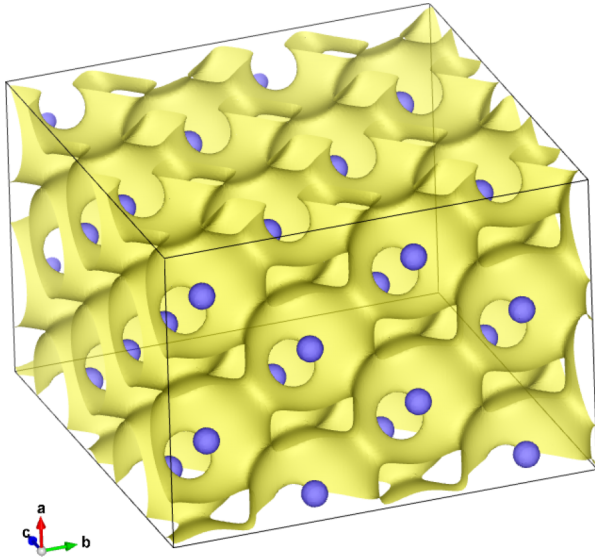
FIG. 9. $Im3m$ isosurfaces of the density profiles for the state $\rho^* = 16.3$, $c = 0.12$ and $\rho_1^*(\mathbf{r}) = 18.0$ (yellow), $\rho_2^*(\mathbf{r}) = 30.1$ (blue), corresponding in both cases to 70% of the peak value. The lengths in reduced units of the axes a, b, and c of the cell displayed in the figure are $a^* \equiv a/R_{11} = 4.09$, $b^* = 5.79$, and $c^* = 5.79$.

FIG. 10. $Im3m$ isosurfaces of the density profiles for the state $\rho^* = 16.3$, $c = 0.7$ and $\rho_1^*(\mathbf{r}) = 142.7$ (yellow), $\rho_2^*(\mathbf{r}) = 17.5$ (blue), corresponding in both cases to 70% of the peak value. The reduced lengths of the cell axes are $a^* = 2.06$, $b^* = 2.92$, and $c^* = 2.92$. The cell has been replicated twice along the a and c directions.

yellow will refer to the density profile of the larger species $\rho_1(\mathbf{r})$ and blue to that of the smaller species $\rho_2(\mathbf{r})$. The coordinates along the directions of the axes a, b, and c of the figures will be denoted by x, y, and z as usual.

In Fig. 9, two density isosurfaces are shown, one for each species, for a state inside the bcc domain at low concentration, namely, $\rho^* = 16.3$ and $c = 0.12$. For this state, the maxima attained by the density profiles of the two species are $\rho_{1,\text{peak}}^* = 25.7$ and $\rho_{2,\text{peak}}^* = 43.0$, and the two isosurfaces correspond to $\rho_1^*(\mathbf{r})/\rho_{1,\text{peak}}^* = \rho_2^*(\mathbf{r})/\rho_{2,\text{peak}}^* = 0.7$. A similar rendition is shown in Fig. 10 for a "specular" state $\rho^* = 16.3$ and $c = 0.70$ in the high-concentration bcc domain with $\rho_{1,\text{peak}}^* = 203.8$ and $\rho_{2,\text{peak}}^* = 25.1$, the isosurfaces being again defined by $\rho_1^*(\mathbf{r})/\rho_{1,\text{peak}}^* = \rho_2^*(\mathbf{r})/\rho_{2,\text{peak}}^* = 0.7$. In both cases, the species at lower concentration is strongly localized at the lattice sites, in such a way that many particles sit on the same site. We can obtain an estimate of the number of particles per cluster n_c by the ratio between the number of particles of the localized species and the number of peaks of the corresponding density profile inside the cell, as already done in Sec. III for the GEM-4 potential. This gives $n_c \simeq 8.4$ for the smaller species in Fig. 9 and $n_c \simeq 22$ for the larger species in Fig. 10. The occurrence of multiple occupancy of the lattice sites is not surprising, given the connection between the presence of a λ-line and cluster formation already stressed in investigations of one-component fluids[11,12] as well as of the same mixture studied here.[20] We note that also the fact that the species at lower concentration arranges into a localized bcc crystal with multiple occupancy is consistent with the results obtained so far for the phase diagram of one-component fluids with $Q^{\pm}$ potentials,[11,12,59] according to which such a phase is the preferred one at the lowest densities at which the system is inhomogeneous.

A less expected feature concerns the behavior of the species at higher concentration which, instead of being localized, is distributed in the region unoccupied by the other species,
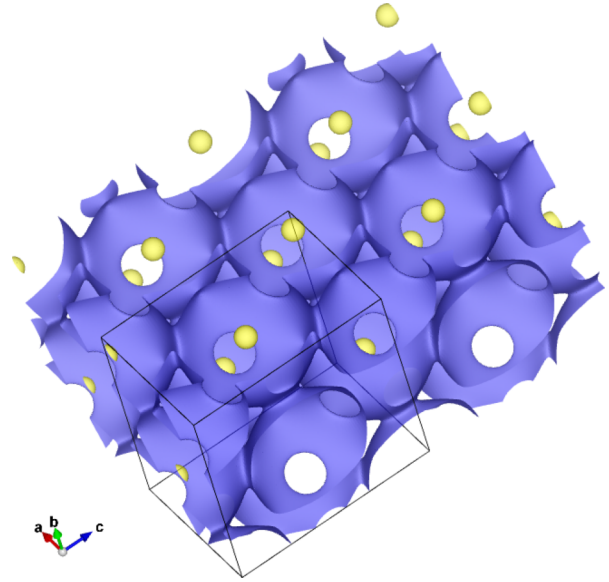
thus forming a percolating network. This situation, implying a strong dissimilarity in the degree of localization of the two species, is in line with the analysis developed at the end of Sec. IV, based on the effective $Q^{\pm}$ interactions between particles of a species due to those of the other. At the same time, it is different from the arrangement considered in Ref. 20, i.e., the CsCl structure, in which a cluster of particles of a species sits at the center of a bcc conventional unit cell, with eight clusters of particles of the other species at the corners, so that both species are located at the sites of a simple cubic (sc) lattice. While this arrangement is certainly favored over the uniform state inside the region bounded by the λ-line where the latter is unstable,[20] what we find here indicates that it is not the actual configuration chosen by the mixture.

In order to make sure that this is not due to the possibility that we might just have missed this structure in the process of minimization of the grand potential, we generated it by the same procedure used in Ref. 20, namely, by describing the density profiles of both species as superpositions of Gaussians of widths α_i for species i centered at the sites of a CsCl lattice with lattice constant a and minimizing the Helmholtz free energy functional per unit volume corresponding to grand potential (1) at fixed densities $\bar{\rho}_i$ with respect to a and α_i. These are the only free parameters since, for given $\bar{\rho}_i$, the amplitudes A_i of the Gaussians are determined by the conditions $\int d^3\mathbf{r}\, \rho_i(\mathbf{r})/V = \bar{\rho}_i$. We then used the density profiles thus obtained as the input of the unconstrained minimization algorithm and performed three sweeps in concentration of the phase diagram at $\rho^* = 12$, $0.2 \leq c \leq 0.7$, $\rho^* = 15$, $0.15 \leq c \leq 0.8$, and $\rho^* = 20$, $0.1 \leq c \leq 0.85$. At all the concentrations considered, save for $c = 0.7$ at $\rho^* = 12$, $c = 0.8$ at $\rho^* = 15$, and $c = 0.85$ at $\rho^* = 20$, for which the uniform state was obtained, the algorithm did converge to a sc structure. This, however, was always found to be metastable with respect to the phases displayed in Fig. 8.

The fact that the CsCl structure is never preferred may at first seem surprising since, as observed in Ref. 20, having clusters of one species sit among eight clusters of the other species appears as the most natural way to arrange the particles in order to take advantage of the mutual affinity between different species. Nevertheless, with the benefit of hindsight, it is easy to come out with an explanation as to why this is not the case: suppose that one considers a state with rather different concentrations of the two species, such as, e.g., those on the low- and high-concentration sides of the λ-line. Since in the CsCl structure the number of clusters is the same for the two species, one expects the local density at the lattice sites to be higher for the more abundant species provided the difference in concentration is large enough, and this is indeed the case for the density profile given by the Gaussian parameterization.

However, *what happens is actually the converse*: as the λ-line is approached, Figs. 6 and 7 show that the local density of particles of species i around a particle of the same species is higher for the *less abundant* species. The same is true for the non-uniform states of Figs. 9 and 10, as evident from the values of $\rho^*_{1,\text{peak}}$ and $\rho^*_{2,\text{peak}}$ reported above. The reason for this behavior is that, unlike particles interacting via $Q^{\pm}$ potentials such as the GEM-4 potential discussed in Sec. III, here the particles of a given species do not have any intrinsic tendency towards cluster formation: this comes about only because of the effective interaction due to the other species, which increases with the density of the latter according to Eq. (35). Hence, when the difference in concentration between the two species is large enough, the effective interaction between particles of the less abundant species will always be stronger than that between particles of the more abundant species, simply because the former is driven by the larger number of particles. An indirect indication of this situation is that in the CsCl structure, where one maintains that the more abundant species should be localized by the less abundant one, the localization is rather weak, as pointed out in Ref. 20 and testified by the very large values of the Lindemann ratio reported there.

In fact, for concentrations of the smaller species $c \gtrsim 0.5$, there are indications that the CsCl state is not even a local minimum of the free energy. This is illustrated in Fig. 11, which displays the density profile of the smaller species $\rho^*_2(\mathbf{r})$ in a single sc cell at $\rho^* = 15$ and $c = 0.6$. Panels (a) and (b)

refer, respectively, to the Gaussian parameterization based on the CsCl structure and to the result of the numerical minimization with the CsCl structure as input. In both cases, $\rho^*_2(\mathbf{r})$ has been visualized by selecting its isosurface such that $\rho^*_2(\mathbf{r}) = \rho^*_{2,\text{peak}}/2$ and halving it by a section at constant x so as to show also the domain where $\rho^*_2(\mathbf{r})$ is larger than $\rho^*_{2,\text{peak}}/2$. When the CsCl state is fed into the numerical minimization algorithm, we find that it still converges to a sc lattice for both species, but at the same time, the density peak of the smaller species becomes strongly anisotropic, splits, and moves from the center to the faces of the cell. Eventually, instead of a structure described by the bcc conventional cell with clusters of the larger and smaller species located at the corners and center of the cell in stoichiometric (cluster) ratio 1 : 1, the arrangement which we obtain is that of the fcc conventional cell with clusters of the larger species at the corners (not shown in the figure), and clusters of the smaller species at the centers of the faces in stoichiometric ratio 1 : 3. As stated above, this structure is still metastable with respect to the bcc phases of Figs. 9 and 10, but we thought it useful to discuss it in order to show how the potential of the CsCl phase for achieving optimal coordination between different species is hindered by the inability of the low-concentration species to confine the high-concentration species. In principle, this leaves the possibility that this structure may still be found at some intermediate concentration, such that either species is capable of confining the other. But the fact that this was not found to be the case suggests that in this regime, the more likely scenario is the converse one, in which *neither* species is capable of confining the other. In fact, nowhere in the phase diagram did we find the occurrence of simultaneous localization of both species at the lattice sites, as one of the species, or even both, as will be illustrated in the following, always percolate in the space left available by the other.

Coming back to the stable bcc phases of Figs. 9 and 10, it should be stressed that, notwithstanding its non-localized character, the percolating species cannot be considered as a nearly uniform background in which the localized species is embedded, the density profile being in fact strongly inhomogeneous for both species. This is best appreciated by considering a contour plot of a section of the profiles which includes the peak region. Figure 12 shows two such plots for the state of
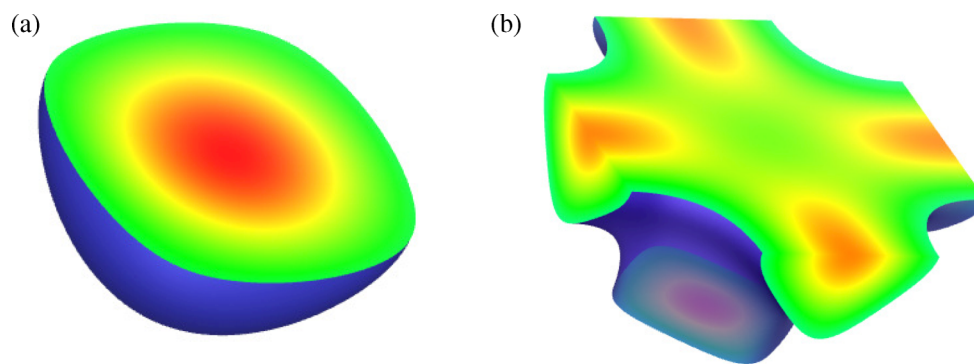
(a)   (b)

FIG. 11. Density profile of the smaller species $\rho^*_2(\mathbf{r})$ at $\rho^* = 15$ and $c = 0.6$ given by a superposition of Gaussians centered at the sites of a CsCl lattice (panel (a)) and by the unconstrained minimization with the CsCl density profile as input (panel (b)). Each panel displays a section of the domain such that $\rho^*_2(\mathbf{r})$ exceeds half of its peak value $\rho^*_{2,\text{peak}}$ on a plane at constant x which includes the peak. Red corresponds to $\rho^*_{2,\text{peak}} = 24.3$ (panel (a)) and $\rho^*_{2,\text{peak}} = 21.5$ (panel (b)). The width of the section in reduced units is 1.14 and 1.50 for panel (a) and (b), respectively. For each panel, the isosurface at $\rho^*_2(\mathbf{r}) = \rho^*_{2,\text{peak}}/2$ has been drawn in blue.
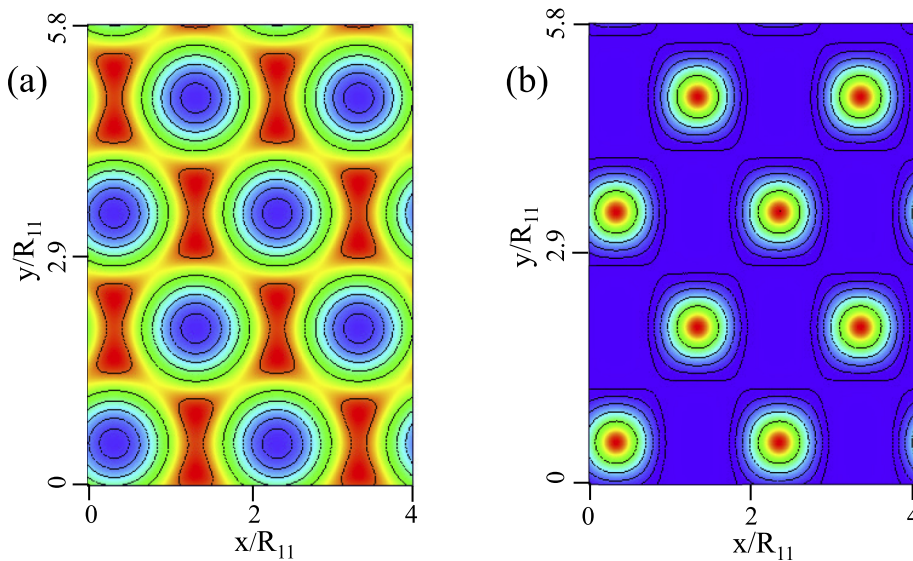
FIG. 12. Contour plots of the density profiles for the state shown in Fig. 9 on a plane perpendicular to the c-axis of the cell, which includes some of the peaks of $\rho_1(\mathbf{r})$ (panel (a)) and $\rho_2(\mathbf{r})$ (panel (b)). Dark red corresponds to the peak values $\rho^*_{1,\text{peak}} = 25.7$ (panel (a)) and $\rho^*_{2,\text{peak}} = 43.0$ (panel (b)). Dark blue corresponds to the minimum values $\rho^*_{1,\text{min}} = 0.44$ (panel (a)) and $\rho^*_{2,\text{min}} = 8.5 \times 10^{-2}$ (panel (b)).

Fig. 9, obtained by cutting the cell along a plane at constant z, with z chosen so as to intercept some of the peaks of $\rho_1(\mathbf{r})$ and $\rho_2(\mathbf{r})$, respectively. The density profiles $\rho_1(\mathbf{r})$ and $\rho_2(\mathbf{r})$ were found to have the same Bravais lattice, namely, the bcc lattice for the states of Figs. 9 and 10. However, in order to describe the positions of the peaks of the percolating species, one also needs to introduce a basis. The symmetry of the structure thus obtained is fully characterized by the space group rather than the Bravais lattice alone. We first determined autonomously the Bravais lattice and the point group, and then identified the space group by the FINDSYM program freely available online.[62] For both states, we found that the density profile belongs to the *Im3m* space group, the same as that of the simple bcc lattice with no basis points which pertains to the localized species. For the percolating species, it corresponds to the primitive bicontinuous cubic phase sometimes referred to as "plumber's nightmare."

As observed above, at both concentrations, the minority species is that which is localized. However, the two species are not completely interchangeable, as the bcc region at high c where the larger species is localized and the smaller species percolates is wider than the corresponding region at low c where the converse is true, and the domain at $c \simeq 0.3$ with respect to which the phase diagram appears roughly symmetric corresponds to a less than equimolar concentration of the smaller species. This means that, as one would expect, the tendency to localize is stronger for the larger species. Nevertheless, the ability to overcome this tendency at suitably low c so as to have the larger particles percolate in a localized crystal of the smaller ones is in stark contrast with the behavior of asymmetric mixtures of hard spheres[60] and represents one more example of the different properties of soft- and hard-core fluids.

As we move further inside the phase diagram from the low- or the high-concentration side, the bcc lattice gives way to the triangular lattice. Figures 13 and 14 depict the density profiles for two "specular" states at $\rho^* = 16.4$, $c = 0.22$ and $\rho^* = 16.5$, $c = 0.51$ lying on either side of the "central" gyroid-diamond region at $c \simeq 0.3$. In the present case in which this does not affect the readability of the figures,

we have represented, in addition to a given isosurface for each species, also the whole domain where the density profile of that species exceeds its value at the isosurface, i.e., the region whose outer boundary coincides with the isosurface, as in Fig. 11. For the state of Fig. 13, we have $\rho^*_{1,\text{peak}} = 34.7$ and $\rho^*_{2,\text{peak}} = 35.0$, and the two isosurfaces correspond to $\rho^*_1(\mathbf{r})/\rho^*_{1,\text{peak}} = \rho^*_2(\mathbf{r})/\rho^*_{2,\text{peak}} = 0.4$. In Fig. 14, we have $\rho^*_{1,\text{peak}} = 88.6$ and $\rho^*_{2,\text{peak}} = 32.6$, and the isosurfaces were chosen again at $\rho^*_1(\mathbf{r})/\rho^*_{1,\text{peak}} = \rho^*_2(\mathbf{r})/\rho^*_{2,\text{peak}} = 0.4$.

Here, unlike in the bcc phases discussed above, there is a direction along which $\rho_1(\mathbf{r})$ and $\rho_2(\mathbf{r})$ are uniform, so that the density profile is doubly rather than triply periodic. In both cases, one species is localized at the sites of an equilateral triangular lattice forming a rod-like arrangement, while the other one percolates in the remaining region in such a way that its
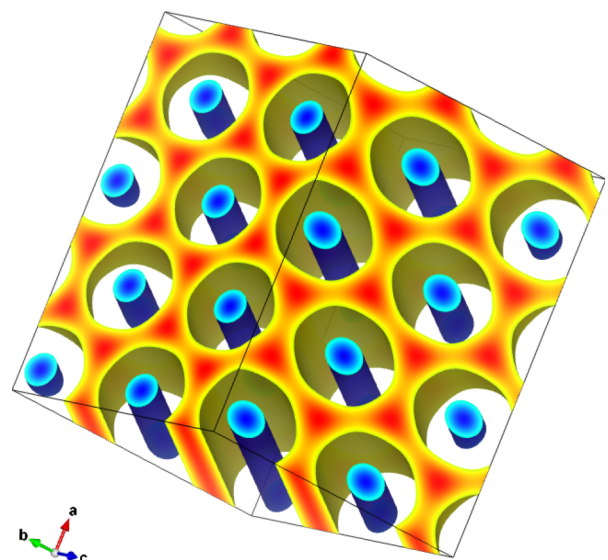

FIG. 13. Sections of the density profiles for the state $\rho^* = 16.4$ and $c = 0.22$ such that $\rho^*_1(\mathbf{r}) \geq 13.9$ (red to yellow) and $\rho^*_2(\mathbf{r}) \geq 14.0$ (dark blue to light blue), corresponding to $\rho^*_1(\mathbf{r})/\rho^*_{1,\text{peak}} \geq 0.4$ and $\rho^*_2(\mathbf{r})/\rho^*_{2,\text{peak}} \geq 0.4$. The reduced lengths of the axes of the cell displayed in the figure are $a^* = 5.88$, $b^* = 4.81$, and $c^* = 4.79$.
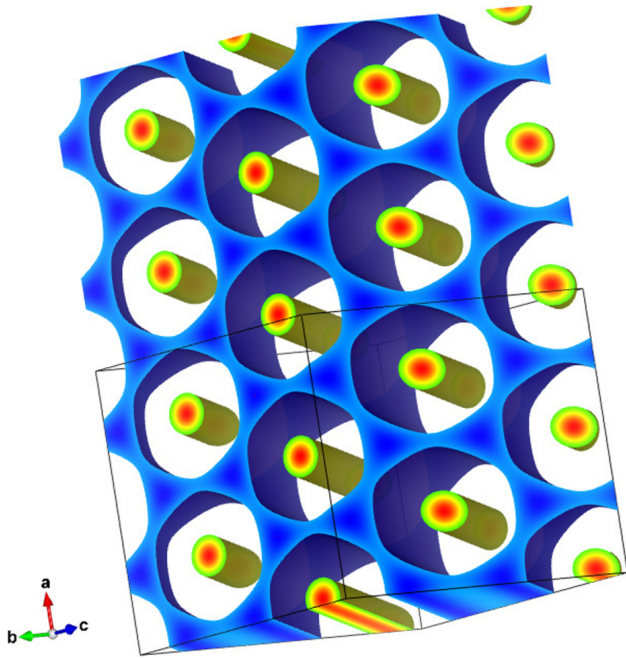
FIG. 14. Sections of the density profiles for the state $\rho^* = 16.5$ and $c = 0.51$ such that $\rho_1^*(\mathbf{r}) \geq 35.4$ (red to green) and $\rho_2^*(\mathbf{r}) \geq 13.0$ (dark blue to light blue), corresponding to $\rho_1^*(\mathbf{r})/\rho_{1,\text{peak}}^* \geq 0.4$ and $\rho_2^*(\mathbf{r})/\rho_{2,\text{peak}}^* \geq 0.4$. The reduced lengths of the cell axes are $a^* = 3.35$, $b^* = 4.11$, and $c^* = 4.11$. The cell has been replicated twice along the a direction.

density peaks form a honeycomb lattice, i.e., a triangular lattice with a two-point basis. As before, the localized or percolating character of a species is dictated by its concentration rather than its size, the localized species being either the smaller or the larger one for states lying, respectively, to the left or to the right of the gyroid-diamond domain. We observe that in both cases, as we move from the outer bcc region to the rod region, the number of particles of the localized species increases, while its density profile at the peak decreases, as shown by the values reported above. Conversely, the number of particles of the percolating species decreases, but the peak of its density profile increases. Therefore, there is a tendency for the localized species to become less localized, and for the percolating species to become more localized.

In fact, as we proceed towards the innermost part of the phase diagram and enter inside the two narrow domains labeled helices I and helices II, the distinction between localized and percolating structure gets blurred. Here, a basis is required in order to describe the positions of the peaks of both species. The Bravais lattice of the helices I phase is non-cubic, namely, face-centered orthorhombic (fco), and the space group is found to be the *Fddd*. Although the structures formed by the two species have the same space group, they do not share the same particle arrangement, as already observed for the bcc and triangular phases. This is shown in Fig. 15, which refers to the state at $\rho^* = 16.4$ and $c = 0.27$ and displays two isosurfaces such that $\rho_1^*(\mathbf{r})/\rho_{1,\text{peak}}^* = 0.75$, $\rho_2^*(\mathbf{r})/\rho_{2,\text{peak}}^* = 0.65$, the peak values being $\rho_{1,\text{peak}}^* = 47.3$, $\rho_{2,\text{peak}}^* = 37.5$. It appears that the smaller particles are no longer localized, but form a rather loose network of threefold-connected nodes[34] which spans the whole cell, leaving large gaps available to the larger particles. The
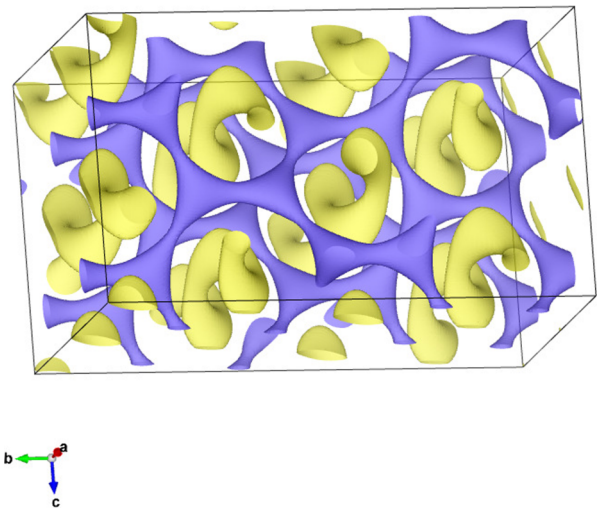

FIG. 15. *Fddd* isosurfaces of the density profiles for the state $\rho^* = 16.4$, $c = 0.27$ and $\rho_1^*(\mathbf{r}) = 35.5$ (yellow), $\rho_2^*(\mathbf{r}) = 24.4$ (blue), corresponding, respectively, to $\rho_1^*(\mathbf{r})/\rho_{1,\text{peak}}^* = 0.75$ and $\rho_2^*(\mathbf{r})/\rho_{2,\text{peak}}^* = 0.65$. The reduced lengths of the axes of the cell displayed in the figure are $a^* = 3.40$, $b^* = 5.71$, and $c^* = 3.37$.

latter occupy the gaps by arranging themselves into a helical structure such that the helices have alternating chirality.

In the helices II domain, the Bravais lattice is again non-cubic, this time body-centered tetragonal (bct) instead of fco. The space group is the $I4_1/amd$ for both species. Figure 16 shows the isosurfaces such that $\rho_1^*(\mathbf{r})/\rho_{1,\text{peak}}^* = 0.25$ and $\rho_2^*(\mathbf{r})/\rho_{2,\text{peak}}^* = 0.75$ for a state in this domain, i.e., $\rho^* = 16.5$ and $c = 0.42$, for which $\rho_{1,\text{peak}}^* = 101.8$ and $\rho_{2,\text{peak}}^* = 32.1$. The situation is qualitatively similar to that found in the fco helices I phase but, not surprisingly, the roles of the larger
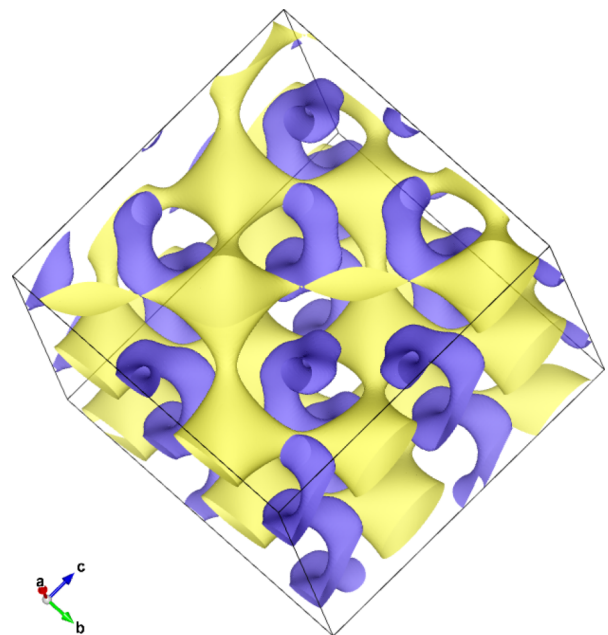

FIG. 16. $I4_1/amd$ isosurfaces of the density profiles for the state $\rho^* = 16.5$, $c = 0.42$ and $\rho_1^*(\mathbf{r}) = 25.4$ (yellow), $\rho_2^*(\mathbf{r}) = 24.1$ (blue), corresponding, respectively, to $\rho_1^*(\mathbf{r})/\rho_{1,\text{peak}}^* = 0.25$ and $\rho_2^*(\mathbf{r})/\rho_{2,\text{peak}}^* = 0.75$. The reduced lengths of the axes of the cell displayed in the figure are $a^* = 3.38$, $b^* = 3.98$, and $c^* = 3.98$.

and smaller species are reversed, as now the smaller species forms the helices which occupy the gaps left available by the network of the larger species. Moreover, the network is now fourfold connected.

We should point out that, for ease of readability, in both Figs. 15 and 16, the helical isosurfaces have been chosen so that the local density at the isosurface is not far from its peak value. This makes evident that there is a preferred direction along which the particles tend to arrange, namely, the winding direction of the helices. Nevertheless, one should also keep in mind that, unlike in the case of the bcc cluster or triangular rod phases discussed above, here the density profile is in fact quite diffuse for both species, as shown more clearly in Fig. 17, which refers to the state $\rho^* = 16.4$ and $c = 0.27$ already considered in Fig. 15 and displays the regions bounded by the isosurfaces $\rho_1^*(\mathbf{r}) = 14.2$ and $\rho_2^*(\mathbf{r}) = 11.2$ such that $\rho_1^*(\mathbf{r})/\rho_{1,\text{peak}}^* = \rho_2^*(\mathbf{r})/\rho_{2,\text{peak}}^* = 0.3$ on two sections perpendicular to the b-axis at $y = 0$ and $y = 1.1R_{11}$, the direction of the helices being that of the a-axis. Much as one may say that the helices formed by species 1 fill the gaps left by species 2 on the basis of Fig. 15, one may as well say, by looking at Fig. 17, that the network formed by species 2 fills the gaps left by species 1, so that actually either species percolates in the voids left available by the other one. In the light of this, it is unlikely that the helices of Figs. 15 and 16 arise simply as a consequence of confinement of species 1 and 2, respectively, inside the pores formed by the other species. Rather, the helical shape is due to the fact that those pores are themselves chiral and therefore act as templates or "threads" for the helices. Figure 17 is also helpful in showing that the helical structure of species 1 results from a deformation of the honeycomb formed by that species in the doubly periodic phase of Fig. 13, while the loose network formed by species 2 results from a deformation of the rods of species 2 in the same doubly periodic phase. This point is perhaps of minor importance, yet we have mentioned it because, if Figs. 13 and 15 were compared without any knowledge of which species

either structure is made of, one would be tempted to view the helices as a deformation of the rods and the open network as a deformation of the honeycomb, thereby assigning them to the wrong species. A similar consideration holds for the comparison between Figs. 14 and 16.

As we finally enter in the central region which acts as the pseudo-symmetry axis of the phase diagram, the distinction between the roles of the two species is lost. This region consists of a gyroid domain at low density and a diamond domain at high density. The Bravais lattice is bcc for the gyroid and fcc for the diamond but, as in the previous cases, the lattice alone does not convey much information on the phase structure. The density profiles for a state in the bcc domain at $\rho^* = 16.4$ and $c = 0.37$ are represented in Fig. 18 by the isosurfaces such that $\rho_1^*(\mathbf{r})/\rho_{1,\text{peak}}^* = \rho_2^*(\mathbf{r})/\rho_{2,\text{peak}}^* = 0.7$, the peak values being $\rho_{1,\text{peak}}^* = 57.2$ and $\rho_{2,\text{peak}}^* = 34.9$. Here, not only does one species percolate in the space left available by the other but also the structure formed by the two species is the same. In this case, we were not able to identity the space group by FINDSYM, but combining the information on the Bravais lattice and the point group left the $I432$ and $I4_132$ as the only possibilities. We then assigned to each isosurface the $I4_132$ space group of the gyroid bicontinuous surface, in the light of the fact that the $I432$ would correspond to a structure much more involved than that which we observed, obtained by no less than eight intertwined gyroid networks.[61] We also remark that the space group which is assigned to the gyroid is often the $Ia3d$, but in fact, this pertains more precisely to the double gyroid, i.e., the surface resulting from the two intertwined networks of Fig. 18, assuming that the networks are identical, so that swapping them leaves the whole surface unchanged. This is clearly not the case in the present situation in which, even though the two species are arranged in the same fashion, they still differ in size and volume fraction. The structure resulting
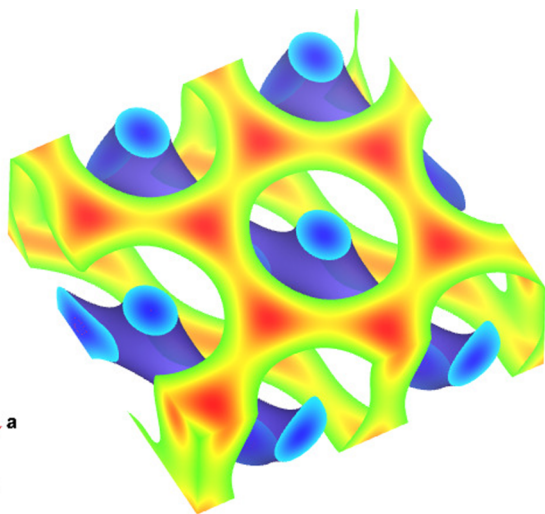

FIG. 17. Density profiles for the state $\rho^* = 16.4$ and $c = 0.27$ already shown in Fig. 15. The figure displays two sections at $y = 0$ (bottom) and $y = 1.1R_{11}$ (top) of the domains such that $\rho_1^*(\mathbf{r}) \geq 14.2$ (red to green) and $\rho_2^*(\mathbf{r}) \geq 11.2$ (dark blue to light blue), corresponding to $\rho_1^*(\mathbf{r})/\rho_{1,\text{peak}}^* \geq 0.3$ and $\rho_2^*(\mathbf{r})/\rho_{2,\text{peak}}^* \geq 0.3$. The isosurface at $\rho_2^*(\mathbf{r}) = 11.2$ (indigo) is also shown.

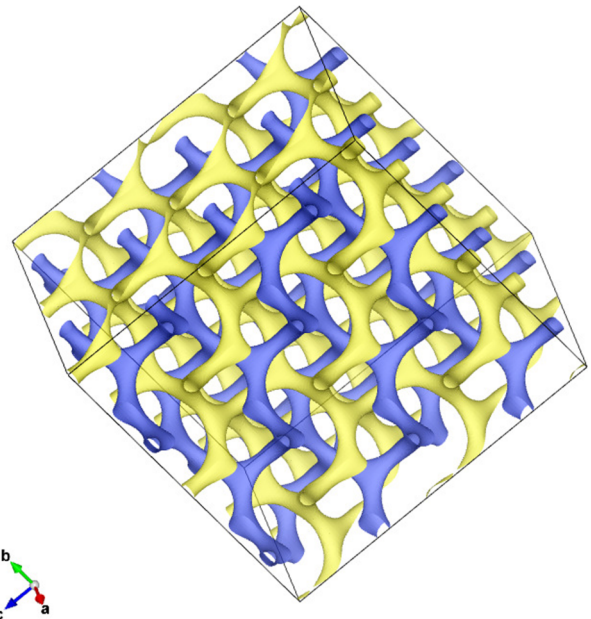FIG. 18. $I4_132$ isosurfaces of the density profiles for the state at $\rho^* = 16.4$, $c = 0.37$ and $\rho_1^*(\mathbf{r}) = 40.1$ (yellow), $\rho_2^*(\mathbf{r}) = 24.4$ (blue), corresponding to $\rho_1^*(\mathbf{r})/\rho_{1,\text{peak}}^* = \rho_2^*(\mathbf{r})/\rho_{2,\text{peak}}^* = 0.7$. The reduced lengths of the axes of the cell displayed in the figure are a* = 4.14, b* = 5.86, and c* = 5.86.
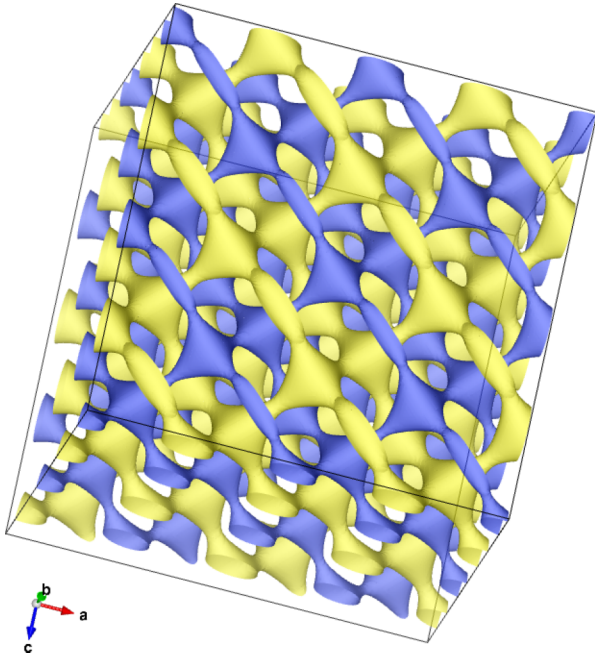
FIG. 19. $Fd3m$ isosurfaces of the density profiles for the state at $\rho^* = 19.8$, $c = 0.33$ and $\rho_1^*(\mathbf{r}) = 44.8$ (yellow), $\rho_2^*(\mathbf{r}) = 29.8$ (blue), corresponding to $\rho_1^*(\mathbf{r})/\rho_{1,\text{peak}}^* = \rho_2^*(\mathbf{r})/\rho_{2,\text{peak}}^* = 0.4$. The reduced lengths of the axes of the cell displayed in the figure are a* = 4.98, b* = 4.98, and c* = 4.98.

from the two species is then referred to as "alternating double gyroid."[63]

The structure of the fcc phase at high density is shown in Fig. 19, which refers to the state at $\rho^* = 19.8$ and $c = 0.33$. The peak values $\rho_{1,\text{peak}}^* = 112.1$ and $\rho_{2,\text{peak}}^* = 74.5$ are considerably higher than those given above for the lower-density gyroid phase. The isosurfaces shown in the figure correspond to $\rho_1^*(\mathbf{r})/\rho_{1,\text{peak}}^* = \rho_2^*(\mathbf{r})/\rho_{2,\text{peak}}^* = 0.4$. As in the gyroid phase, the two species share the same structure, namely, that of the diamond $Fd3m$ surface. If the difference between the two species is disregarded so as to view the two mutually interpenetrating networks as interchangeable, the double diamond $Pn3m$ surface is obtained. In the present situation, "alternating double diamond" would be a more precise name.

B. Discussion of the phase diagram

The qualitative description of the phase diagram given above prompts a number of comments. First, we notice that several features of the scenario just described are not new, but have in fact been known for quite some time in a closely related context, i.e., the phase behavior of block copolymers. It is well known that diblock copolymer melts exhibit microphase separation, which has been studied by DFT[26,38] and SCFT[2,25,35] based on an effective free-energy functional. In those approaches, the melt is considered incompressible, so that the density is not a relevant thermodynamic variable, but, unlike in the present case, the system is not athermal. The phase diagram is then a function of the polymer composition, which has the same meaning as the concentration c in this study, and the product χN of the Flory parameter χ times the degree of polymerization N. The parabolic shape of the phase diagram in the χN-c plane is similar to that of the phase diagram of Fig. 8

in the ρ^*-c plane. In fact, for diblock copolymers in which monomers of different species are assumed to occupy the same volume, the phase diagram is strictly symmetric with respect to the $c = 0.5$ axis. In the innermost region, a lamellar phase is predicted. As one moves out of this region by either decreasing or increasing the concentration, one meets first a gyroid phase, then a triangular phase of cylindrical rods, then a cubic bcc phase, and finally the homogeneous fluid.[25,26] It should also be remarked that recently effective DFT and SCFT approaches have predicted essentially the same sequence of phases in fluids with competing short-range attractive and longer-range repulsive interactions,[8–10] in which the inverse temperature and the density play the roles of the variables χN and c in block copolymer melts (in Ref. 9, a $Fddd$ phase was found instead of the gyroid, but that was traced back in the same paper to the approximations inherent to the effective DFT).

The cubic bcc and triangular phases have the same structure and are found in the same sequence as those obtained here at low and high concentrations (the triangular doubly periodic phase is generally referred to as "hexagonal," but here the term "triangular" has been preferred in order to avoid confusion with the hexagonal Bravais lattice in three dimensions). However, in the region at intermediate concentration, the phase portrait is rather different from the present one: in block copolymers, the gyroid phase is squeezed in two narrow domains between the lamellar and the triangular phases, whereas here the gyroid shares with the diamond the innermost region of the phase diagram, which in block copolymers is assigned to the lamellar phase. The phase diagram of Fig. 8 also presents two domains whose shape and position are similar to those of the gyroid phase in block copolymers, but they are instead occupied by the two non-cubic fco and bct phases.

One can then say that, compared to block copolymers, the Gaussian mixture displays bicontinuous phases in a significantly larger domain of the phase diagram. Here, we will not try to elucidate the reason of such an interesting behavior, aside of the obvious remark that this system differs from block copolymers in three respects: First, there is no connectivity; second, its compressibility is non-vanishing; and third, particles of different species are more compatible (or less incompatible) with each other than those of the same species. The above observation that the same sequence of phases displayed by block copolymers has been reported also in fluids of unconnected particles with competing interactions[8,10] indicates that lack of connectivity alone is not sufficient to explain the behavior found here. We leave this point to future investigation.

As for the fco and bct phases, it is interesting to observe that, as stated in Sec. I, experiments in triblock[39] and diblock[40] copolymers as well as theoretical SCFT calculations[34] have shown the occurrence of an orthorhombic $Fddd$ phase similar to that of the fco helices I region discussed here; although for diblock copolymers, it is predicted to be stable only in a very small domain of the phase diagram.[34] The possibility of a stable tetragonal $I4_1/amd$ phase like that predicted in the helices II region has also been suggested.[64]

As observed at the beginning of this section, the lamellar phase does not appear in the phase diagram of Fig. 8. This does not mean that this phase is actually never found; in fact, it can be easily obtained by functional minimization starting from a

trial density profile which is non-uniform along a single direction. However, it is always preempted by other phases, with a lower grand potential per unit volume at given chemical potentials. Its absence may be surprising, because Fig. 8 suggests that the λ-line and the boundary between the homogeneous and the inhomogeneous fluids merge at the point at which they reach their minimum, thereby leading to a second-order transition. On the other hand, an analysis based on a Landau effective functional shows that in such a case, the modulated phase should necessarily be of lamellar type.[7,38] The same kind of Landau functional is recovered by expanding functional (1) in powers of the deviations $\delta\rho_\alpha(\mathbf{r})$ of the density profile from the homogeneous state and truncating the expansion at fourth order. Therefore, one would expect that also in the present system, a lamellar phase should exist in some domain of Fig. 8 which includes the minimum, similarly to what is predicted for block copolymers.[25,26,38]

Nevertheless, this apparent inconsistency disappears upon closer inspection of the phase diagram, which shows that, even in the very neighborhood of the minimum of the λ-line, the transition from the homogeneous to the inhomogeneous regions remains first order, although very weakly so. This is displayed in Fig. 20, where the square of the order parameter A of the two species has been plotted as a function of density at constant concentration $c = 0.4$. Following the lines of Refs. 7, 28, and 42, A has been defined as the amplitude of the largest Fourier component of $\rho_\alpha(\mathbf{r})$ at $k \neq 0$, normalized by that of the component at $k = 0$. As one crosses the border between the homogeneous fluid and the inhomogeneous triangular phase, A^2 does not vanish, but reaches for both components a small value between 0.005 and 0.01. These correspond, respectively, to reduced densities $\rho^* = 9.95$, for which the triangular phase is metastable with respect to the homogeneous fluid, and $\rho^* = 9.99$, for which the triangular phase prevails. We also observe that A^2 as a function of ρ^* deviates appreciably from linearity, whereas for a second-order transition, the mean-field theory used here would give a linear dependence on ρ^*.[28,42]

The situation illustrated above bears some resemblance with the modifications undergone by the phase diagram of
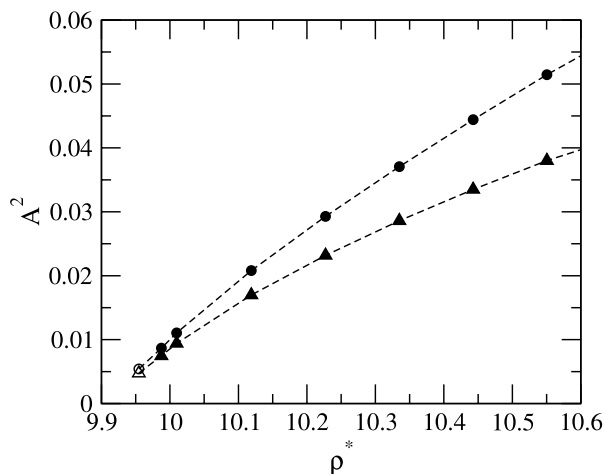

FIG. 20. Square of the normalized amplitude of the density modulation for the triangular phase at $c = 0.4$ across the order-disorder boundary. Circles and triangles refer to species 1 and 2, respectively. The open symbols lie in the disordered-fluid region. The dashed lines are a guide for the eye.

diblock copolymers upon inclusion of the fluctuations in the Landau functional.[65] Fluctuations have the effect of making the order-disorder transition first-order everywhere, including the point at symmetric concentration $c = 0.5$. Moreover, they also imply that this transition can involve different kinds of microphases, while for $c \neq 0.5$, mean-field Landau theory always predicts a disorder-bcc transition.[38] However, in the present case, these features are not due to fluctuations, which our mean-field functional does not include either, but rather to the fact that such a functional includes terms of all orders in $\delta\rho_\alpha(\mathbf{r})$. Specifically, even at the low-density boundary of the phase diagram, where the mean-field Landau functional would predict a second-order transition because of the vanishing of the third-order term in the free energy, odd powers beyond third order can stabilize a first-order transition. This scenario is relevant to the binary Gaussian mixture studied here, but does not apply to block copolymers, whose free energy is symmetric around $c = 0.5$.[38]

A general remark which applies to the whole phase diagram is that, at a given thermodynamic state, the local minima of the free energy corresponding to different phases are generally very close to each other. For instance, if we consider a state well inside the diamond phase, such as the state at $\rho^* = 19.8$ and $c = 0.33$ to which Fig. 19 refers, we find that the modulus of the relative difference between its grand potential per unit volume and that of the lamellar phase at the same chemical potentials μ_1 and μ_2 amounts to $\sim 8 \times 10^{-4}$. If we compare the diamond with the gyroid, this difference further decreases to $\sim 4 \times 10^{-5}$, even though the above state is rather far from the phase boundary. We have checked that these small differences are not affected by the details intrinsic to the numerical minimization, such as the number of points at which the density profile is discretized, or the choice of the trial density profile used to start the minimization. Such a close competition is a characteristic of microphases and implies that for a specified functional form of the density profile, the class of functions among which the minimization is performed can also play a role. For instance, in Ref. 26, the phase behavior of block copolymers was investigated by an effective Landau-Brazovskiĭ functional,[66] and it was shown that, in order to recover a stable gyroid phase, Fourier expansion (15) of the density profile must include at least the nearest- and next-nearest-neighbor shells in reciprocal space. Truncation at the nearest-neighbor shell yields only the bcc, triangular, and lamellar phases. In this respect, the minimization method which we have employed is clearly an asset.

While it is reassuring that the algorithm can resolve small differences in the thermodynamic potential, we cannot nevertheless rule out the possibility that moving to a different free-energy functional, e.g., by keeping fluctuations into account, could alter this delicate balance of very closely competing phases, thereby modifying the phase portrait. The experimental counterpart of this situation is that the most stable phase could easily be preempted by metastable phases of similar free energy.

We must also recall that, as stated in Sec. II B, in the present investigation, we have assumed that the axes which define the unit cell where the density profile is sampled are mutually orthogonal. Therefore, it is natural to ask to which

extent the results presented here are affected by this assumption. We then performed a stability check, in which we used as the input density profiles those of the phases described above, but allowed the angles between the axes to change in the course of the minimization and found that the algorithm converged to the same structures which were provided on input. Although this does not rule out the possibility that trigonal, monoclinic, or triclinic phases may exist and even prove to be more stable than some of those which we have found here, at least it shows that the latter are genuine minima of the free-energy functional, i.e., their stability is not an artifact which would disappear as soon as tilted unit cells are introduced.

C. Cluster formation

Another topic worth considering is how cluster formation in one-component fluids of particles interacting via $Q^\pm$ potentials such as the GEM-4 potential studied in Sec. III compares with the same process in the Gaussian mixture, for those states in which the latter system gives localized clusters similar to those obtained in the former. To this end, we focused on the bcc phase at high concentration in the phase diagram of Fig. 8 where, as shown in Fig. 10, the particles of the larger species 1 arrange into localized clusters of spherical shape. We have performed a sweep of that phase by changing the density at fixed concentration $c = 0.6$, and in Fig. 21, we have plotted as a function of ρ_1 the nearest-neighbor distance d, the number of particles per cluster n_c, and the localization parameter σ already displayed in Fig. 5 for the GEM-4 potential.
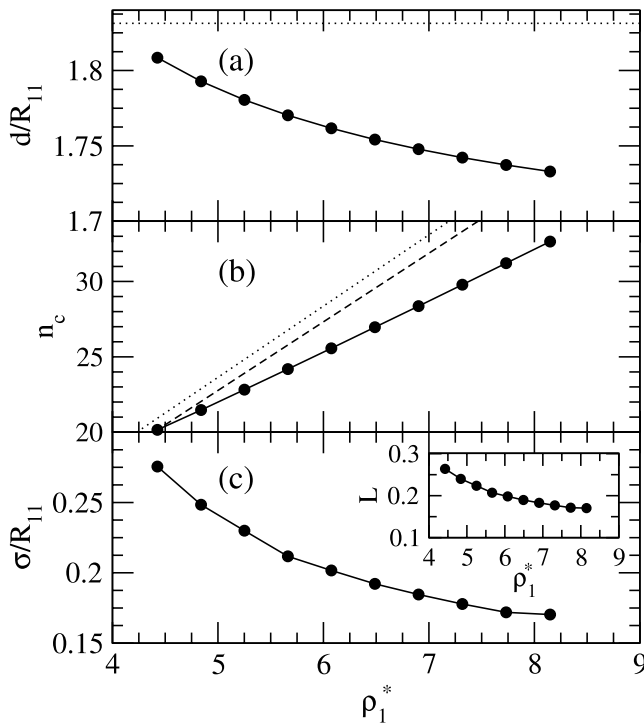

FIG. 21. Distance between nearest-neighbor clusters d (panel (a)), number of particles per cluster n_c (panel (b)), and localization parameter σ (panel (c)) for the localized bcc phase of the Gaussian mixture at $c = 0.6$, as a function of the reduced density of the localized species ρ_1^*. The inset in panel (c) is the Lindemann ratio $\sqrt{3}\sigma/d$. Symbols and lines as in Fig. 5.

Panel (a) shows that also in the present case, the quantity $d_\lambda = \pi\sqrt{6}/k_\lambda$ obtained from the wave vector k_λ on the λ-line provides a reasonable estimate of d. However, while k_λ, and thus d_λ, hardly change along the high-concentration branch of the λ-line, the actual d does show a dependence on density which, albeit still weaker than in atomic crystals with single-site occupancy, is nevertheless appreciably stronger than in the GEM-4 potential. Specifically, d is a monotonically decreasing function of ρ_1^*, so that an increase in the density is achieved not only by increasing the occupation number n_c of the lattice sites as in $Q^\pm$ interactions but also by decreasing at the same time the distance between lattice sites d as in atomic crystals. Hence, as ρ_1 increases, n_c increases less steeply than what is predicted by Eq. (28) with a constant d.

This is shown in panel (b), where n_c is compared with the linear behavior of Eq. (28), with γ set at the value $\gamma = 4\sqrt{3}/9$ of the bcc lattice, and d determined as in Fig. 5 either from its value at the point at lowest density or by setting $d = d_\lambda$. Unlike in the corresponding panel of Fig. 5, deviations from the behavior expected for fixed d are significant.

A further comparison with the GEM-4 potential concerns the localization parameter displayed in panel (c), obtained as in Fig. 5 by fitting each peak to a Gaussian of variance σ, and the Lindemann ratio $L = \sqrt{3}\sigma/d$ displayed in the inset. The qualitative behavior is similar in the two cases, the density profile becoming more and more localized as the density is increased, with σ always considerably smaller than the characteristic particle size R_{11}. In fact, as far as the Gaussian mixture is concerned, we note that the clusters are more strongly localized than they are in the metastable CsCl structure discussed in Sec. V A: in the latter case, for $\rho^* = 20$, the minimum value of L of species 1 is above 0.3, as shown in Fig. 3 of Ref. 20. This minimum is located at $c \simeq 0.6$ and thus corresponds to $\rho_1^* \simeq 8$, near the point at highest ρ_1^* of Fig. 21, which has $L = 0.17$. However, for the GEM-4 potential, the degree of localization is even stronger, since its reduced localization parameter σ/R at a given reduced density ρ^* is nearly three times smaller, and the Lindemann ratio more than two times smaller, than the corresponding quantities of the Gaussian mixture at the same reduced density of the localized species ρ_1^*. In order to compensate for this, the density profile attains much higher peaks in the GEM-4 case, even though the overall number of particles per cluster n_c is smaller than in the Gaussian mixture. For instance, at the highest density $\rho^* \simeq \rho_1^* = 8.15$ plotted in Figs. 5 and 21, the peak of the reduced density profile of the Gaussian mixture is about $\rho_{1,\text{peak}}^* \simeq 4 \times 10^2$, while that of the GEM-4 fluid is one order of magnitude higher, $\rho_{\text{peak}}^* \simeq 4 \times 10^3$.

Overall, one can say that in the Gaussian mixture, the predilection for a specific value of the inter-cluster distance d is not so extreme as in the GEM-4 fluid: compared to the latter, d has more freedom to adjust itself in response to a change of density, and within a given cluster, the particles are allowed to spread over a wider region. This has to be traced back to the fact that, as discussed in Secs. III and IV, for the GEM-4 fluid, clustering is determined by the pair interaction alone and the value of d is basically intrinsic to the system, whereas for the Gaussian mixture, the formation of clusters of a given species is due to the effective, state-dependent interaction mediated by

the other species. The above observation is consistent with a former study[67] of a binary mixture of Gaussian and GEM-4 particles, in which the density profiles of the two species were described by superpositions of Gaussians centered at the sites of two identical cubic lattices shifted from each other, and the clusters formed by the Gaussian particles were again found to be considerably less localized than those formed by the GEM-4 particles.

Nevertheless, the results that we have reported here show that, even for Gaussian particles, the local density at its peak values cannot certainly be considered small, its order of magnitude ranging between ∼10 and ∼10^2 in reduced units. If these particles are to represent polymers in solution, one must then require that the polymers be long enough for the system to be still considered in the semi-dilute regime, otherwise its modelization in terms of an effective Gaussian pair interaction is questionable.

VI. CONCLUSIONS

A. Overview of the results

We have developed a DFT minimization approach tailored to periodic structures and have employed it to study the phase diagram of a model binary Gaussian mixture, which can be regarded as a rough modelization of a mixture of two homopolymers with negative non-additivity of their radii of gyration.

There are two main conclusions that we draw from this investigation: First, this class of mixtures deserves perhaps more attention than it has received so far. Choosing a specific realization of this model with, admittedly, no insight other than the fact that its ability to form microphases had already been established in a former study[20] uncovered all the phases commonly predicted and observed in block copolymer melts, namely, the primitive bcc *Im3m*, the equilateral triangular or hexagonal, and the gyroid *I4₁32* (double gyroid *Ia3d* if the two species are regarded as equivalent), except for the lamellar phase, which was always superseded by other, more stable structures. In addition, we obtained the diamond *Fd3m* phase (double diamond *Pn3m* for equivalent species) and two non-cubic phases, namely, an orthorhombic *Fddd* phase which has been predicted[34] and observed in diblock[40] and triblock[39] copolymers not long ago, as well as a tetragonal *I4₁/amd* phase whose existence has been conjectured,[64] but to our knowledge has not been reported so far in block copolymers, either theoretically or experimentally. In the latter phases, neither species can be considered localized, since each of them percolates in the voids left available by the other. However, unlike in the gyroid and diamond phases, the structures of the two species are different. In particular, one of the species forms a rather loose network with large pores and the other species is preferentially, although not exclusively, located inside these pores, forming helices. This is likely to be due to the chirality of the pores themselves, which thus act as a template for the growth of the helices. A similar occurrence is found in inorganic compounds such as zeolites, whose ability to form chiral channels has been intensively investigated and is one of the main reasons for the interest in this class of materials.[68] It is interesting that these chiral structures can be obtained from a system with purely

isotropic interactions such as the present one, although in our case, no net chirality results, since the helices have opposite handedness.

A general observation which applies to the whole phase diagram is that whether localization takes place or not is ultimately dictated by concentration: if the concentration c of the smaller species is made suitably low, one obtains a localized phase of the smaller species inside a percolating phase of the larger species, which mirrors that obtained at high c, in which the roles of the two species are reversed. This reversibility is made possible by the soft-core nature of the repulsive interaction: in mixtures of asymmetric hard spheres, a crystal of the larger species embedded in a matrix of the smaller species does occur, but the converse arrangement does not.[60] As one moves towards the inner region of the phase diagram, the distinction between the localized and percolating phases becomes more and more blurred and is eventually lost; when c is around ∼0.35, the two species form in fact the same kind of structure, either gyroid or diamond depending on the total density. It is worth pointing out that the region where bicontinuous phases are expected to occur is substantially wider here than in block copolymers, in which they are predicted in two narrow domains squeezed between the triangular and lamellar phases.[25,26] This is a noticeable result, because bicontinuous phases have prospects for interesting applications.[41]

Like one-component fluids with $Q^{\pm}$ potentials, the Gaussian mixture considered here supports multiple occupancy of the lattice sites. However, this system manages to increase its density by both increasing the site occupation number and decreasing the lattice spacing at the same time. As a consequence, the rate at which the number of particles per cluster increases with density and the degree of localization of the particles within a given cluster are lower than in $Q^{\pm}$ potentials. This is true for the GEM-4 interaction which has been used here for a comparison and would be true *a fortiori* for $Q^{\pm}$ potentials such as those proposed to model two-body effective interactions in ring polymers[57] or amphiphilic dendrimers,[15,16] which have a local minimum at $r = 0$. In fact, in a DFT study[59] of the double-Gaussian interaction of Ref. 16, it was found that the lattice constant actually *increases* on increasing the density, albeit slightly so. This implies that the rate at which particles accumulate in the local minimum of the interaction is so high that a system of given volume can afford to lose some of its lattice sites and still support an increase of its total number of particles.

Hence, with $Q^{\pm}$ potentials, the local particle density within a given cluster becomes rapidly very high as the average density is increased. Since these potentials come about as a modelization of two-body effective interactions obtained by atomistic simulations of an isolated pair of polymers, one may ask whether they will still give a realistic description of an assembly of such polymers, at densities at which many-body contributions to the effective interactions are expected to become important. In Ref. 57, it was found that for ring polymers, these contributions modify the effective interaction to the point that cluster formation does not occur. A subsequent study[69] showed that in amphiphilic dendrimers, the formation of cluster crystals does instead take place, yet with some relevant

qualitative differences with respect to the picture based on the sole pair potential. In this respect, the weaker increase of the cluster population with the average density found in Gaussian mixtures can be considered as an asset, since it suggests that mixtures of linear polymers or non-amphiphilic dendrimers may lend themselves to be more accurately described than ring polymers or amphiphilic dendrimers by purely two-body effective interactions such as those considered here.

Besides the intrinsic interest of Gaussian mixtures as a model system for microphase formation, the other main conclusion that we draw from the present study is that the ability to uncover the rich phase behavior displayed by this system rests crucially on the procedure which we have employed to minimize the free-energy functional. Specifically, we did not make any *a priori* assumption on the functional form of the density profile $\rho(\mathbf{r})$ aside of requiring it to be periodic and performed an unconstrained optimization by sampling $\rho(\mathbf{r})$ on a large number of points, such that both the values of $\rho(\mathbf{r})$ at these points *and* the axes of the unit cell which identify the Bravais lattice were regarded as variational parameters. The comparison with the results which we had obtained in a previous investigation[28] shows that inclusion of the cell axes in the optimization is of paramount importance in order to prevent $\rho(\mathbf{r})$ from getting stuck in non-periodic, metastable states, especially for triply periodic structures.

For one-component fluids interacting via $Q^{\pm}$ potentials such as the GEM-4 considered in Sec. III and the double Gaussian considered in Ref. 59, it turns out that the use of the unconstrained minimization is an overkill that adds little or no further information to what is obtained by representing $\rho(\mathbf{r})$ as a superposition of Gaussians centered at the sites of several simple Bravais lattices and choosing the lattice which corresponds to the lowest free energy. However, this is no longer true in the present case, because it would have been very difficult (at least to us) to have any inkling of the configurations actually chosen by the system, and we would have failed to include most of them in the search of the most stable structure. Moreover, even if we had known in advance which configurations to expect, the problem of representing them analytically would still have been there: instances in which one species percolates in the space left available by the other one, possibly forming intertwined structures with strongly anisotropic densities, do not lend themselves to be well represented by a superposition of Gaussians localized at given lattice sites, unless the lattice is supplemented with a basis which may consist of a significant number of points, at positions yet to be specified. In such a situation, leaving the system the freedom to choose its preferred arrangement in an unbiased way is clearly an asset well worth the effort. The strategy which we have adopted here to accomplish this program is rather general, since it does not require the free-energy functional to assume mean-field form (1) and can be implemented also for different functionals as well as, of course, for non-Gaussian interactions.

B. Open problems and perspectives

There are also some questions that are prompted by this study: First and foremost, the phase diagram and the description of the particle arrangements in the different phases

presented here refer to a single, specific choice of the potential parameters $\epsilon_{\alpha\gamma}$ and $R_{\alpha\gamma}$ for the strengths and ranges of the interactions. One might then ask how the phase portrait would be affected by a change of these parameters, even assuming that one restricts oneself to those situations in which microphase formation is expected. Although this question comes naturally, providing a complete answer is a rather formidable task which we have not attempted to pursue here. In an investigation that we will report elsewhere, we focused on symmetric Gaussian mixtures such that $\epsilon_{11} = \epsilon_{22}$ and $R_{11} = R_{22}$, which offer the advantage of a reduced number of interaction parameters and are also of some interest as their invariance with respect to the exchange of the two species is shared with the usual modelization of block copolymers. For this system, we found that the existence of the λ-line requires negative non-additivity, and that if the degree of non-additivity is sufficiently high, the spinodal does not exist, as in the case of the asymmetric mixture which has been studied here. For lower non-additivity, the spinodal line is present, and this can lead to a different topology of the phase diagram, possibly featuring both microphase formation and a bulk demixing transition in the same mixture. The results which we have obtained so far indicate that the details of the phase diagram, such as the location and the structure of the phases which inhabit the inhomogeneous region, are probably rather sensitive to the specific choice of the ranges and strengths of the interactions, especially as one moves far from the λ-line.

Another issue which arises naturally, but to which it is difficult to give a fully satisfactory answer, is the possibility that, at least in some regions of the phase diagram, the phases described here might be superseded by yet further configurations, which we might have been unable to detect. Here, it has been assumed that the unit cell can be represented by a set of mutually orthogonal vectors. As discussed in Sec. II B, we reckoned that the additional flexibility granted by a tilted cell would have as a downside to increase the instances in which a given structure is obtained time and again as the same density profile sampled over different cells. Nevertheless, leaving the angles between the axes as variables to be optimized alongside with the axis lengths is fully feasible. In fact, we did implement such an extension of the algorithm and used it to check that the structures obtained here are locally stable with respect to a deformation of the cell. We also observe that the assumption of orthogonal axes of the *unit* cell does not necessarily rule out the occurrence of any structure whose *primitive* cell is not described by orthogonal lattice vectors, e.g., the triangular phase, which was indeed observed. Nevertheless, undetected trigonal, monoclinic, or triclinic configurations of lower free energy might still be looming somewhere. For instance, trigonal phases were found by genetic algorithms in the phase diagram of both star polymers[45] and ionic microgels.[45–47] In the future, we might want to include the angles in the functional minimization from the beginning, although we must keep in mind that the inability of ruling definitely out the existence of other phases more stable than those which have been observed is intrinsic to systems whose free-energy landscape is characterized by many local minima. Here, the search of the (hopefully) global minimum for a given thermodynamic state has been done simply by starting the minimization from

many different trial density profiles and following different minimization paths. In principle, other, more sophisticated methods to single out the most stable structure among the local minima obtained by the algorithm could be implemented, such as those mentioned in Sec. II B.

Notwithstanding the rather naive search of the global free energy minima performed here, the ability of the algorithm to find the local minima in an unbiased way with no hint as to their functional form holds a potential for a number of applications. For instance, one could consider microphase formation in one-component hard-core fluids with competing short-range attractive and longer-range repulsive interactions. The phase diagram of this model fluid has already been thoroughly studied in two dimensions.[6,7] In three dimensions, some general features of the phase diagram were obtained by combining numerical simulation and integral-equation theories,[70] and a detailed investigation of the structure of microphases was subsequently carried out by means of effective free-energy functionals,[8–10] which uncovered essentially the same sequence of microphases (bcc-triangular-gyroid-lamellae) previously found in block copolymer models.[25,26,38] It would be interesting to see whether application of the present DFT will also predict the same scenario.

Another possibility could be the investigation of the effect of an external periodic potential on microphase formation. For instance, the anisotropy induced by the potential might give rise to particle arrangements different from the structures which would be formed spontaneously.

A further development worth pursuing consists in the extension of the method developed here to a curved substrate, e.g., a spherical surface, in order to describe the formation and arrangement of microphases on a membrane or a colloidal particle.[71,72] An ensemble of such "dressed" particles can be regarded as a system of patchy particles that lately have been receiving much attention as a means to engineer anisotropic interactions.[73]

ACKNOWLEDGMENTS

APPENDIX: DETAILS OF THE MINIMIZATION ALGORITHM

The minimization algorithm that we have used is based on the steepest descent, Eqs. (25) and (26). The derivatives $\partial \beta \omega_D / \partial \rho_{\mathbf{n},\alpha}$ and $\partial \beta \omega_D / \partial h_i$ needed in these equations are straightforwardly determined from Eq. (22),

$$\frac{\partial \beta \omega_D}{\partial \rho_{\mathbf{n},\alpha}} = \frac{1}{N^3} \left[\ln(\rho_{\mathbf{n},\alpha}/\bar{\rho}_\alpha) - \beta \mu_\alpha^{ex} \right]$$
$$+ \frac{1}{N^6} \sum_{\mathbf{m},\gamma} e^{-2\pi i \mathbf{n}\cdot\mathbf{m}/N} \hat{\rho}_{\mathbf{m},\gamma} \beta \tilde{w}_{\alpha\gamma}(\mathbf{k_m}), \quad (A1)$$

$$\frac{\partial \beta \omega_D}{\partial h_i} = \frac{1}{N^6} \sum_{\mathbf{m},\alpha,\gamma} \hat{\rho}_{\mathbf{m},\alpha} \hat{\rho}_{-\mathbf{m},\gamma} \frac{d\beta \tilde{w}_{\alpha\gamma}}{d(k^2)}(\mathbf{k_m}) \, h_i m_i^2. \quad (A2)$$

With respect to the basic steepest descent, however, several improvements were introduced in order to increase the efficiency of the algorithm. First, in Eq. (25), use of preconditioning has been made via the Jacobi preconditioner. In practice, this means that Eq. (25) has been replaced by

$$\rho_{\mathbf{n},\alpha}^{k+1} = \rho_{\mathbf{n},\alpha}^k - \eta \xi_{\mathbf{n},\alpha}^k, \quad (A3)$$

where the quantities $\xi_{\mathbf{n},\alpha}^k$ are defined as

$$\xi_{\mathbf{n},\alpha}^k = \frac{\partial \beta \omega_D}{\partial \rho_{\mathbf{n},\alpha}}\bigg|_k \left(\frac{\partial^2 \beta \omega_D}{\partial \rho_{\mathbf{n},\alpha}^2}\bigg|_k \right)^{-1} \quad (A4)$$

and the second derivative $\partial^2 \beta \omega_D / \partial \rho_{\mathbf{n},\alpha}^2$ is given by

$$\frac{\partial^2 \beta \omega_D}{\partial \rho_{\mathbf{n},\alpha}^2} = \frac{1}{N^3} \frac{1}{\rho_{\mathbf{n},\alpha}} + \frac{1}{N^6} \sum_{\mathbf{m}} \tilde{w}_{\alpha\alpha}(\mathbf{k_m}). \quad (A5)$$

The purpose of this modification is to deform long and narrow basins of attraction, for which the steepest descent may become very inefficient, so as to make them less elongated.

Moreover, following the conjugate gradient method, the direction of descent does not coincide with that of the set $\xi_{\mathbf{n},\alpha}^k$, but is determined by a linear combination of the $\xi_{\mathbf{n},\alpha}$ at all previous steps according to

$$\rho_{\mathbf{n},\alpha}^{k+1} = \rho_{\mathbf{n},\alpha}^k - \eta \psi_{\mathbf{n},\alpha}^k, \quad (A6)$$

where $\psi_{\mathbf{n},\alpha}^k$ is given by the following recurrence relations:

$$\psi_{\mathbf{n},\alpha}^k = \xi_{\mathbf{n},\alpha}^k + \zeta_{k,\alpha} \psi_{\mathbf{n},\alpha}^{k-1}, \quad (A7)$$

$$\zeta_{k,\alpha} = \frac{\sum_{\mathbf{n}} \xi_{\mathbf{n},\alpha}^k \left(\xi_{\mathbf{n},\alpha}^k - \xi_{\mathbf{n},\alpha}^{k-1} \right)}{\sum_{\mathbf{n}} \left(\xi_{\mathbf{n},\alpha}^{k-1} \right)^2}. \quad (A8)$$

Use of (preconditioned) conjugate gradient method (A6) generally increases the efficiency of the computation with respect to (preconditioned) steepest descent (A3), but occasionally may prove less robust. Therefore, it is wise not to use Eq. (A6) throughout, but to insert a steepest descent step by using Eq. (A3) instead of Eq. (A6) every N iterations, where N was typically set at $N = 10$ or $N = 50$. We have not used either preconditioning or conjugate directions in Eq. (26) for the cell axes, since these are the quantities which mostly affect the convergence; hence, robustness was put before computational speed.

The quantities $\rho_{\mathbf{n},\alpha}$ and h_i were updated according to Eqs. (A6) and (26) until the partial derivatives $\partial \beta \omega_D / \partial \rho_{\mathbf{n},\alpha}$ and $\partial \beta \omega_D / \partial h_i$ were found to be vanishing within a prescribed accuracy. Specifically, the iteration was stopped when the quantity $N^3 \sum_{\mathbf{n},\alpha}(\partial \beta \omega_D^* / \partial \rho_{\mathbf{n},\alpha}^*)^2 + \sum_i (\partial \beta \omega_D^* / \partial h_i^*)^2$ became smaller than 10^{-15}, where the asterisks denote the reduced quantities $\omega_D^* \equiv \omega_D R_{11}^3$, $\rho_{\mathbf{n},\alpha}^* \equiv \rho_{\mathbf{n},\alpha} R_{11}^3$, and $h_i^* \equiv h_i R_{11}$. We remark that because of expressions (A1) and (A2) of the partial derivatives, the above quantity is independent of N in the large-N limit.

Irrespective of the details of the minimization technique, i.e., preconditioned vs. non-preconditioned or conjugate vs. simple gradients, we found that the step-size parameters η, δ in Eqs. (A6) and (26) must be chosen with care, or else convergence would be so slow that the whole algorithm

would become useless. The optimal choice of η and δ at a given step would be determined by the minimum of $g_k(\eta, \delta) \equiv \beta\omega_D(\rho^k_{n,\alpha} - \eta\psi^k_{n,\alpha}, h^k_i - \delta\phi^k_i)$, regarded as a function of η and δ at fixed $\rho^k_{n,\alpha}$, $\psi^k_{n,\alpha}$, h^k_i, ϕ^k_i, where $\psi^k_{n,\alpha}$ is given by Eqs. (A7) and (A8), and $\phi^k_i = \partial\beta\omega_D/\partial h_i|_k$ according to Eq. (26). This does not lead to explicit expressions for η and δ, but the minimum may be determined iteratively by solving the equations $\partial g_k/\partial\eta = 0$ and $\partial g_k/\partial\delta = 0$ via the Raphson-Newton method. A single Raphson-Newton step gives

$$
\eta_k = \left(-\frac{\partial^2 g_k}{\partial\delta^2}\frac{\partial g_k}{\partial\eta} + \frac{\partial^2 g_k}{\partial\eta\partial\delta}\frac{\partial g_k}{\partial\delta} \right)
$$
$$
\times \left[\frac{\partial^2 g_k}{\partial\eta^2}\frac{\partial^2 g_k}{\partial\delta^2} - \left(\frac{\partial^2 g_k}{\partial\eta\partial\delta}\right)^2 \right]^{-1}\Bigg|_{\eta,\delta=0}, \quad (A9)
$$

$$
\delta_k = \left(-\frac{\partial^2 g_k}{\partial\eta^2}\frac{\partial g_k}{\partial\delta} + \frac{\partial^2 g_k}{\partial\eta\partial\delta}\frac{\partial g_k}{\partial\eta} \right)
$$
$$
\times \left[\frac{\partial^2 g_k}{\partial\eta^2}\frac{\partial^2 g_k}{\partial\delta^2} - \left(\frac{\partial^2 g_k}{\partial\eta\partial\delta}\right)^2 \right]^{-1}\Bigg|_{\eta,\delta=0}. \quad (A10)
$$

In practice, we disregarded the off-diagonal contributions in Eqs. (A9) and (A10) and determined η and δ as

$$
\eta_k = -\frac{\partial g_k}{\partial\eta}\left(\frac{\partial^2 g_k}{\partial\eta^2}\right)^{-1}\Bigg|_{\eta,\delta=0}, \quad (A11)
$$

$$
\delta_k = -\frac{\partial g_k}{\partial\delta}\left(\frac{\partial^2 g_k}{\partial\delta^2}\right)^{-1}\Bigg|_{\eta,\delta=0}. \quad (A12)
$$

This actually amounts to disregarding the effects of a change in either variable when searching for the minimum with respect to the other. Such a decoupling was preferred over complete Raphson-Newton step (A9) and (A10) because, although in principle less efficient, it was nevertheless found to be more robust. The derivatives of g_k needed in Eqs. (A11) and (A12) are given by

$$
\frac{\partial g}{\partial\eta} = -\sum_{n,\alpha}\frac{\partial\beta\omega_D}{\partial\rho_{n,\alpha}}\psi_{n,\alpha}, \quad (A13)
$$

$$
\frac{\partial^2 g}{\partial\eta^2} = \sum_{l,n,\alpha,\gamma}\frac{\partial^2\beta\omega_D}{\partial\rho_{l,\alpha}\partial\rho_{n,\gamma}}\psi_{l,\alpha}\psi_{n,\gamma}, \quad (A14)
$$

$$
\frac{\partial g}{\partial\delta} = -\sum_i\frac{\partial\beta\omega_D}{\partial h_i}\phi_i, \quad (A15)
$$

$$
\frac{\partial^2 g}{\partial\delta^2} = \sum_{i,j}\frac{\partial^2\beta\omega_D}{\partial h_i\partial h_j}\phi_i\phi_j, \quad (A16)
$$

where we have understood that all the quantities at the rhs of Eqs. (A13)–(A16) are evaluated at $\rho^k_{n,\alpha}$ and h^k_i and have omitted the index and apex k for brevity. Equations (A13) and (A15) are straightforwardly evaluated using the expressions of $\partial\beta\omega_D/\partial\rho_{n,\alpha}$ and $\partial\beta\omega_D/\partial h_i$ given in Eqs. (A1) and (A2). The derivatives $\partial^2\beta\omega_D/(\partial h_i\partial h_j)$ needed in Eq. (A16) are immediately obtained from Eq. (A2),

$$
\frac{\partial^2\beta\omega_D}{\partial h_i\partial h_j} = \frac{1}{N^6}\sum_{m,\alpha,\gamma}\hat\rho_{m,\alpha}\hat\rho_{-m,\gamma}
$$
$$
\times \left[\frac{d^2\beta\tilde{w}_{\alpha\gamma}}{d(k^2)^2}(k_m)\,2m_i^2 n_j^2 h_i h_j + \frac{d\beta\tilde{w}_{\alpha\gamma}}{d(k^2)}(k_m)\,m_i^2\delta_{ij} \right]. \quad (A17)
$$

In order to evaluate Eq. (A14), it is convenient to use direct space for the ideal part of $\beta\omega_D$ and Fourier space for its excess part as in Eq. (22), and we get

$$
\frac{\partial^2 g}{\partial\eta^2} = \frac{1}{N^3}\sum_{n,\alpha}\frac{1}{\rho_{n,\alpha}}\psi^2_{n,\alpha} + \frac{1}{N^6}\sum_{m,\alpha,\gamma}\beta\tilde{w}_{\alpha\gamma}(k_m)\hat\psi_{m,\alpha}\hat\psi_{-m,\gamma}, \quad (A18)
$$

where the hats denote as before the discrete Fourier transform defined in Eq. (20). Use of Eqs. (A11) and (A12) for the step-size amplitudes η and δ leads to a remarkable increase in the speed of convergence with respect to that obtained with a fixed step-size. In principle, one could also make more than just one Raphson-Newton step for each given minimization step k by iterating Eqs. (A11) and (A12) at fixed k, but we have not done so, since we have not found this to bring any significant improvement.

An algorithm similar to that described here was applied to functional minimization in a different context,[74] and also in that case, the use of an adaptive step-size proved crucial to increase the convergence rate. However, one should keep in mind that while the functional considered in Ref. 74 is globally convex in the physical region, this is not the case with present functional (22). Therefore, Eqs. (A11) or (A12) might also lead to a negative step-size. In order to avoid such a potentially catastrophic occurrence, a fixed, positive value for η or δ was used whenever Eqs. (A11) or (A12) would give a negative value.

Moreover, the quantities $\rho^{k+1}_{n,\alpha}$ must obviously be positive if they are to represent physical densities, but this condition is not automatically fulfilled by Eq. (A6). Therefore, $\rho^{k+1}_{n,\alpha}$ was set to a small, positive quantity whenever Eq. (A6) leads to a negative result. This somewhat rough prescription is sufficient to steer Eq. (A6) away from the unphysical region and eventually make it converge to positive values.

[1]M. Seul and D. Andelman, Science **267**, 476 (1995).
[2]M. W. Matsen, J. Phys.: Condens. Matter **14**, R21 (2002).
[3]G. Gompper and M. Schick, *Self-Assembling Amphiphilic Systems* (Academic Press, 1994).
[4]L. E. Scriven, Nature **263**, 123 (1976).
[5]W. M. Gelbart, R. P. Sear, J. R. Heath, and S. Chaney, Faraday Discuss. **112**, 299 (1999); R. P. Sear, S.-W. Chung, G. Markovich, W. M. Gelbart, and J. R. Heath, Phys. Rev. E **59**, R6255 (1999).
[6]A. Imperio and L. Reatto, J. Phys.: Condens. Matter **16**, S3769 (2004); J. Chem. Phys. **124**, 164712 (2006).
[7]A. J. Archer, Phys. Rev. E **78**, 031402 (2008).
[8]A. Ciach, Phys. Rev. E **78**, 061505 (2008); A. Ciach and W. T. Góźdź, Condens. Matter Phys. **13**, 23603 (2010); A. Ciach, J. Pekalski, and W. T. Góźdź, Soft Matter **9**, 6301 (2013).
[9]H. Shin, G. M. Grason, and C. D. Santangelo, Soft Matter **5**, 3629 (2009).
[10]K. von Konigslow, E. D. Cardenas-Mendez, R. B. Thompson, and K. Ø. Rasmussen, J. Phys.: Condens. Matter **25**, 325101 (2013).
[11]B. M. Mladek, D. Gottwald, G. Kahl, M. Neumann, and C. N. Likos, Phys. Rev. Lett. **96**, 045701 (2006); **97**, 019901 (2006).
[12]C. N. Likos, B. M. Mladek, D. Gottwald, and G. Kahl, J. Chem. Phys. **126**, 224502 (2007).
[13]B. M. Mladek, P. Charbonneau, and D. Frenkel, Phys. Rev. Lett. **99**, 235702 (2007).
[14]C. N. Likos, A. Lang, M. Watzlawek, and H. Löwen, Phys. Rev. E **63**, 031206 (2001).
[15]B. M. Mladek, G. Kahl, and C. N. Likos, Phys. Rev. Lett. **100**, 028301 (2008).
[16]D. A. Lenz, B. M. Mladek, C. N. Likos, G. Kahl, and R. Blaak, J. Phys. Chem. B **115**, 7218 (2011).

[17]J. Dautenhahn and C. K. Hall, Macromolecules **27**, 5399 (1994).

[18]A. A. Louis, P. G. Bolhuis, J. P. Hansen, and E. J. Meijer, Phys. Rev. Lett. **85**, 2522 (2000).

[19]C. N. Likos, S. Rosenfeldt, N. Dingenouts, M. Ballauff, P. Lindner, N. Werner, and F. Vögtle, J. Chem. Phys. **117**, 1869 (2002); I. O. Götze, H. M. Harreis, and C. N. Likos, *ibid.* **120**, 7761 (2004).

[20]A. J. Archer, C. N. Likos, and R. Evans, J. Phys.: Condens. Matter **16**, L297 (2004).

[21]A. A. Louis, P. G. Bolhuis, and J. P. Hansen, Phys. Rev. E **62**, 7961 (2000); R. Finken, J. P. Hansen, and A. A. Louis, J. Stat. Phys. **110**, 1015 (2003).

[22]A. J. Archer and R. Evans, Phys. Rev. E **64**, 041501 (2001).

[23]A. J. Archer and R. Evans, J. Phys.: Condens. Matter **14**, 1131 (2002).

[24]I. O. Götze, A. J. Archer, and C. N. Likos, J. Chem. Phys. **124**, 084901 (2006).

[25]M. W. Matsen and M. Schick, Phys. Rev. Lett. **72**, 2660 (1994).

[26]V. E. Podneks and L. W. Hamley, JETP Lett. **64**, 617 (1996).

[27]F. H. Stillinger, Phys. Rev. E **59**, 48 (1999).

[28]M. Carta, D. Pini, A. Parola, and L. Reatto, J. Phys.: Condens. Matter **24**, 284106 (2012).

[29]See, for instance, W. H. Press, S. A. Teukolsky, W. T. Vetterling, and B. P. Flannery, *Numerical Recipes*, 2nd ed. (Cambridge University Press, 1992).

[30]R. B. Thompson, T. Jebb, and Y. Wen, Soft Matter **8**, 9877 (2012).

[31]M. Parrinello and A. Rahman, Phys. Rev. Lett. **45**, 1196 (1980).

[32]C. A. Tyler and D. C. Morse, Macromolecules **36**, 8184 (2003).

[33]J. L. Barrat, G. H. Fredrickson, and S. W. Sides, J. Phys. Chem. B **109**, 6694 (2005).

[34]C. A. Tyler and D. C. Morse, Phys. Rev. Lett. **94**, 208302 (2005).

[35]M. W. Matsen, Eur. Phys. J. E **30**, 361 (2009).

[36]F. J. Martinez-Veracoechea and F. A. Escobedo, Macromolecules **42**, 9058 (2006).

[37]R. B. Thompson, Phys. Rev. E **73**, 020502(R) (2006).

[38]L. Leibler, Macromolecules **13**, 1602 (1980).

[39]T. S. Bailey, C. M. Hardy, T. H. Epps, and F. S. Bates, Macromolecules **35**, 7007 (2002); T. H. Epps, E. W. Cochran, T. S. Bailey, R. S. Waletzko, C. M. Hardy, and F. S. Bates, *ibid.* **37**, 8325 (2004).

[40]M. Takenaka, T. Wakada, S. Akasaka, S. Nishitsuji, K. Saijo, H. Shimizu, M. I. Kim, and H. Hasegawa, Macromolecules **40**, 4399 (2007); M. I. Kim, T. Wakada, S. Akasaka, S. Nishitsuji, K. Saijo, H. Hasegawa, K. Ito, and M. Takenaka, *ibid.* **41**, 7667 (2008).

[41]C. N. Walker, K. C. Bryson, R. C. Hayward, and G. N. Tew, ACS Nano **8**, 12376 (2014).

[42]A. J. Archer, C. Ionescu, D. Pini, and L. Reatto, J. Phys.: Condens. Matter **20**, 415106 (2008).

[43]M. Frigo and S. G. Johnson, Proc. IEEE **93**, 216 (2005).

[44]C. N. Likos, N. Hoffmann, H. Löwen, and A. A. Louis, J. Phys.: Condens. Matter **14**, 7681 (2002).

[45]D. Gottwald, G. Kahl, and C. N. Likos, J. Chem. Phys. **122**, 204503 (2005).

[46]D. Gottwald, C. N. Likos, G. Kahl, and H. Löwen, Phys. Rev. Lett. **92**, 068301 (2004).

[47]D. Gottwald, C. N. Likos, G. Kahl, and H. Löwen, J. Chem. Phys. **122**, 074903 (2005).

[48]See, for instance, C. J. Pickard and R. J. Needs, J. Phys.: Condens. Matter **23**, 053201 (2011).

[49]J. P. K. Doye, D. J. Wales, and M. A. Miller, J. Chem. Phys. **109**, 8143 (1998).

[50]S. Goedecker, J. Chem. Phys. **120**, 9911 (2004).

[51]K. Zhang, P. Charbonneau, and B. M. Mladek, Phys. Rev. Lett. **105**, 245701 (2010).

[52]T. Neuhaus and C. N. Likos, J. Phys.: Condens. Matter **23**, 234112 (2011).

[53]N. B. Wilding and P. Sollich, EPL **101**, 10004 (2013).

[54]N. B. Wilding and P. Sollich, J. Chem. Phys. **141**, 094903 (2014).

[55]M. Schmidt, J. Phys.: Condens. Matter **11**, 10163 (1999).

[56]A. J. Archer and R. Evans, J. Chem. Phys. **118**, 9726 (2003).

[57]A. Narros, A. J. Moreno, and C. N. Likos, Soft Matter **6**, 2435 (2010).

[58]K. Momma and F. Izumi, J. Appl. Crystallogr. **44**, 1272 (2011).

[59]D. Pini, Trans. R. Norw. Soc. Sci. Lett. **3**, 99 (2014).

[60]M. Dijkstra, R. van Roij, and R. Evans, Phys. Rev. E **59**, 5744 (1999).

[61]M. Saba, M. D. Turner, K. Mecke, M. Gu, and G. E. Schröder-Turk, Phys. Rev. B **88**, 245116 (2013).

[62]H. T. Stokes and D. M. Hatch, J. Appl. Crystallogr. **38**, 237 (2005).

[63]M. R. J. Scherer, *Double-Gyroid-Structured Functional Materials* (Springer, 2013).

[64]G. E. Schröder-Turk, A. Fogden, and S. T. Hyde, Eur. Phys. J. B **54**, 509 (2006).

[65]G. H. Fredrikson and E. Helfand, J. Chem. Phys. **87**, 697 (1987).

[66]S. A. Brazovskiǐ, Sov. Phys. JETP **41**, 85 (1975).

[67]S. D. Overduin and C. N. Likos, J. Chem. Phys. **131**, 034902 (2009).

[68]X. Zou, T. Conradsson, M. Klingstedt, M. S. Dadachov, and M. O'Keeffe, Nature **437**, 716 (2005); J. Sun, C. Bonneau, A. Cantín, A. Corma, M. J. Díaz-Cabañas, M. Moliner, D. Zhang, M. Li, and X. Zou, *ibid.* **458**, 1154 (2009).

[69]D. A. Lenz, R. Blaak, C. N. Likos, and B. M. Mladek, Phys. Rev. Lett. **109**, 228301 (2012).

[70]A. J. Archer and N. B. Wilding, Phys. Rev. E **76**, 031501 (2007).

[71]A. M. Jackson, J. W. Myerson, and F. Stellacci, Nat. Mater. **3**, 330 (2004).

[72]E. E. Edlund, O. Lindgren, and M. N. Jacobi, Soft Matter **10**, 2955 (2014).

[73]E. Bianchi, R. Blaak, and C. N. Likos, Phys. Chem. Chem. Phys. **13**, 6397 (2011).

[74]D. Pini, A. Parola, J. Colombo, and L. Reatto, Mol. Phys. **109**, 2989 (2011).